Breakthrough in aluminum protection: Electrochemical and wear insights into sol-gel sealed PEO-coated AA2024-T3 and AA2198-T851

Sajjad Akbarzadeh [a,b,*], Rafael Emil Klumpp [a], Alexandre Mégret [a,b], Vedi Ölmez [c], Véronique Vitry [b], Marie-Georges Olivier [a]

[a] Materials Science Department, Faculty of Engineering, University of Mons, 20, Place du Parc, 7000 Mons, Belgium
[b] Metallurgy Department, Faculty of Engineering, University of Mons, 20, Place du Parc, 7000 Mons, Belgium
[c] Belgian Ceramic Research Centre (BCRC), Avenue Gouverneur Cornez 4, B-7000 Mons, Belgium

ARTICLE INFO

ABSTRACT

In consideration of the intrinsic porosity in layers generated via the plasma electrolytic oxidation (PEO) process, sol-gel coatings have gained a lot of attention for their environmentally friendly and robust protective qualities when applied as a post-treatment. The sealing capabilities of the sol-gel layer were scrutinized for the PEO coating applied on AA2024-T3 and AA2198-T851 aluminum alloys. Electrochemical Impedance Spectroscopy (EIS) and Field Emission Scanning Electron Microscopy (FE-SEM) confirmed that for the same operating conditions, the morphological properties of the PEO coating depend on the substrate nature and play a key role in the corrosion protection given by such duplex coatings. Furthermore, the findings indicated that the use of a sol-gel enhances the wear resistance compared to the blank substrates and the PEO coatings.

1. Introduction

Widely employed in the aerospace sector, the 2xxx aluminum alloys are recognized for their high strength [1,2]. In these alloys, during the solidification process, insoluble intermetallic particles (IM) are generated [3]. In AA2024-T3 alloy, two primary types of particles emerge including the S-phase, consisting of Al_2CuMg, and particles containing Fe, Cu, Al, and Mn expressed as $Al_6(Cu, Mn, Fe)$. These particles serve as vital initiation sites for localized corrosion. Specifically, in chloride-containing environments, a preferential dissolution of aluminum and magnesium occurs, resulting in the enrichment of copper within the IM particles [4–7]. Incorporating 1 wt% of lithium into the aluminum alloy results in a notable enhancement of its elasticity modulus with a density reduction of approximately 3 % [8,9]. The AA2198-T851 alloy stands as a representative of third-generation aluminum alloys, characterized by its composition comprising elements such as Al, Cu, and Li, alongside traces of Mg, Ag, and Zn [10]. The introduction of lithium induces precipitation hardening through the development of diverse strengthening precipitates, including δ′ (Al_3Li), θ′ (Al_2Cu), and T1 (Al_2CuLi) [11]. On the other hand, this alloy exhibits a high vulnerability to localized corrosion, primarily marked by the preferential attack on specific grains and grain boundaries [12].

To overcome the localized corrosion in such alloys, some strategies have been reported in which surface treatment plays an important role [13]. Conversion coatings [14], chemical vapor deposition (CVD) [15], physical vapor deposition (PVD) [16], thermal spraying [17], ion implantation [18], diffusion treatment [19], anodization [20], and PEO [21] are suggested as some surface modification techniques. PEO plays a crucial role in various processes owing to its environmentally friendly properties and its capability to produce dense ceramic coatings on lightweight metals [22]. When it comes to applications that demand wear resistance, PEO coatings demonstrate greater benefits than both hard-chrome plating and hard anodizing [23].

Utilized as an efficient and cost-effective surface treatment, PEO has been applied to different light alloys, including Al [24], Mg [25], and Ti [26]. In contrast to anodizing, this technique involves higher voltage, leading to species diffusion, plasma reactions, and electrochemical reactions. The PEO process typically employs an alkaline aqueous electrolyte, making it a more ecologically sustainable alternative compared to anodizing technology [27,28]. Throughout the PEO process, numerous transient micro-arcs spontaneously emerge on the surface, significantly elevating the pressure and temperature in localized areas. As sparks occur across the working electrode, the oxide layer is inclined to undergo repeated melting and solidification, facilitating its
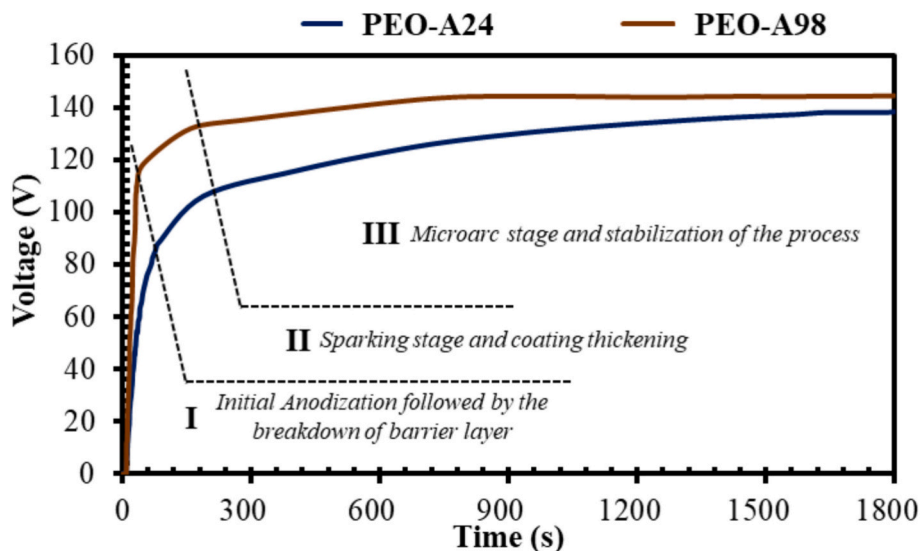
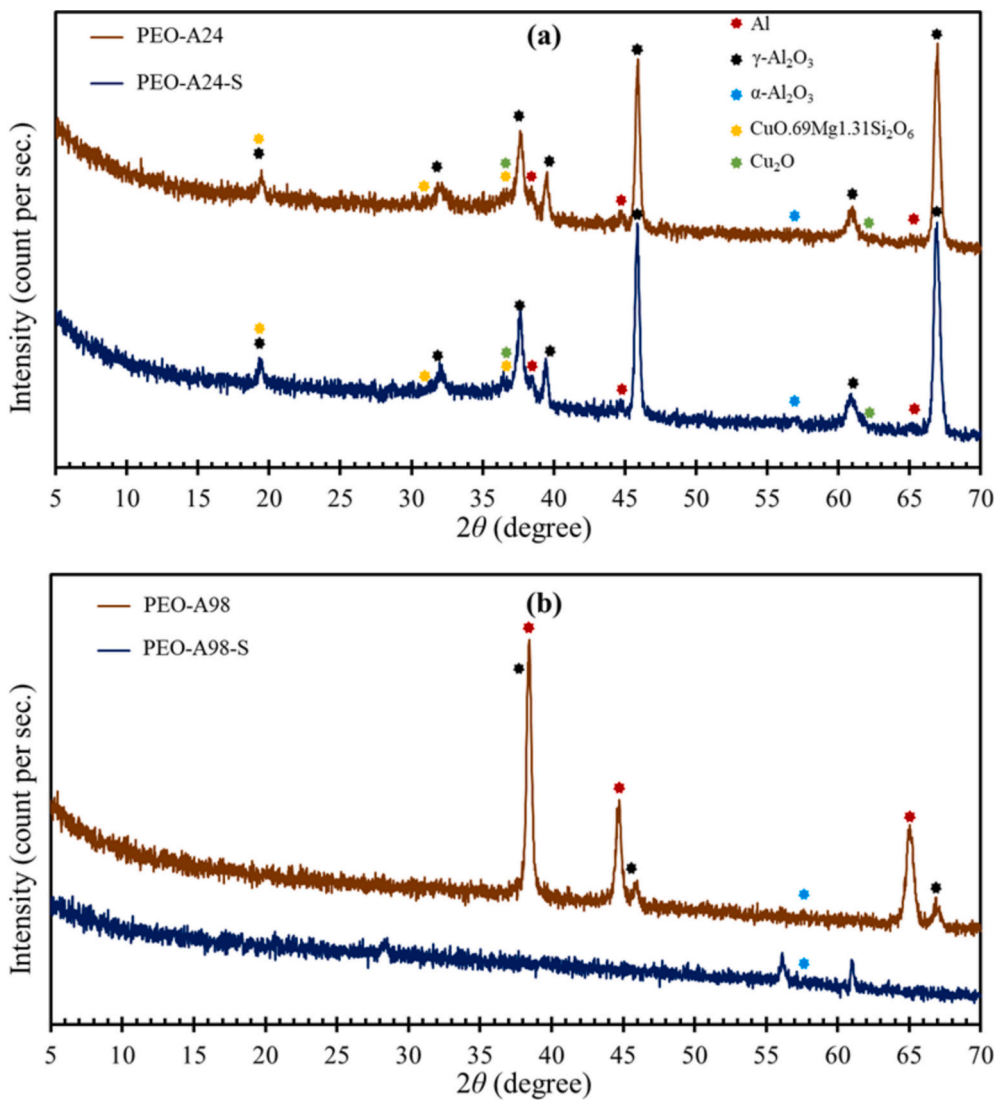**Fig. 1.** Voltage-time curves for PEO-A24 and PEO-A98 during the PEO process.

Fig. 2. GIXRD outcome for PEO-A24 and PEO-A24-S (a) as well as PEO-A98 and PEO-A98-S (b).
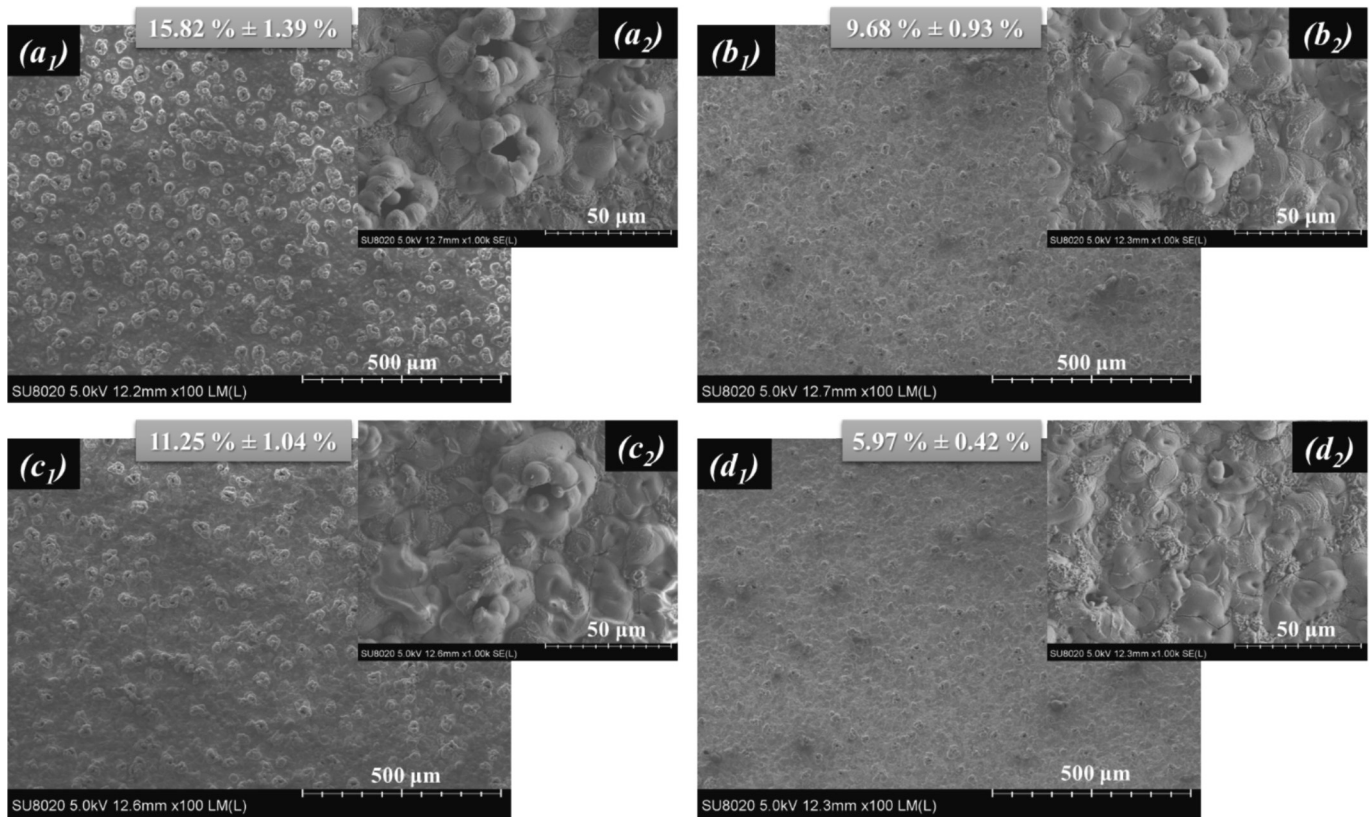
Fig. 3. Planar FE-SEM images (in two magnifications) as well as the proportion of the porosity assessment area of PEO samples corresponded to PEO-A24 (a_1 and a_2), PEO-A98 (b_1 and b_2), PEO-A24-S (c_1 and c_2), and PEO-A98-S (d_1 and d_2).

integration with the constituents of the electrolyte, and developing high-temperature phases [29,30]. Therefore, a coating with improved corrosion protection properties, wear resistance, and hardness is created. Specifically, the PEO layer applied on aluminum alloys comprises a dense layer and a porous layer, with the presence of pores and cracks in the latter being viewed as a limitation for applications requiring long-term protection [31].

Various post-treatments, such as hydrothermal treatments and conversion coatings, might precipitate low-soluble compounds, which can block the intrinsic pores of a PEO layer [32–34]. Application of a sol-gel coating has emerged as a viable technique among surface post-treatments because of its flexible processing, ease of production, and environmental friendliness [35–39]. Sol-gel characteristics are influenced by various factors, including sol-gel precursor, solvent type, solution pH, and aging [40–42]. Nevertheless, the sublayer properties and surface topography are of great importance for the performance of such coatings. Any sol-gel coatings adsorb either chemically or physically to the substrate [43]. In chemical adsorption, covalent bonds are formed by condensation reactions between the hydroxyl groups of surface and hydrolyzed sol-gel molecules [44]. On the other hand, physical adsorption deals with mechanical interlocking, improving adherence between the substrate and the sol-gel coating. As it is well-documented, the PEO porosity is a crucial factor influencing the characteristics and effectiveness of duplex coatings, such as the PEO/sol-gel coating system. [45]. Pezzato et al. [46] confirmed the dissimilar deposition of the sol-gel layer as a post-treatment for PEO coatings on two alloys (AA7020 and AZ80), caused by the distinct morphology of the PEO coatings.

This study aims to investigate how the substrate and corresponding PEO morphology impact the sealing effectiveness of a specific sol-gel top layer. PEO coatings were applied to both AA2198-T851 and AA2024-T3 aluminum alloys, using identical electrical parameters and electrolyte composition. To the best of the authors' knowledge, no prior research

has focused on producing PEO coatings on the AA2198-T851 alloy. The presence of lithium in the AA2198-T851 alloy significantly influences the development of the PEO coating, which is discussed in this investigation. Subsequently, PEO coatings on both aluminum alloys were coated with a sol-gel layer to examine how the PEO morphology as well as the substrate affect the properties of the PEO/sol-gel duplex coating system. The sol-gel precursors were tetraethyl orthosilicate (TEOS) and 3-glycidoxypropyltrimethoxysilane (GPTMS) in which the TEOS moiety plays a pivotal role in the creation of sol-gel networks due to its four hydrolyzable bonds. When combined with the GPTMS molecule, featuring one epoxide end group and three hydrolyzable branches, it facilitates effective pore-filling capabilities in the network [47]. Various characterization techniques such as Field Emission Scanning Electron Microscopy (FE-SEM) and Grazing Incidence X-ray diffraction (GIXRD) were conducted to scrutinize the PEO coatings in the presence/absence of sol-gel sealing. Moreover, the corrosion resistance properties as well as the mechanical features like tribological properties were examined.

2. Materials and methods

Two grades 2xxx aluminum alloys, AA2024-T3 (4.5 % Cu, 1.41 % Mg, 0.61 % Mn, 0.12 % Fe, 0.03 % Zn, and Al balance (wt%)) and AA2198-T851 (3.31 % Cu, 0.96 % Li, 0.31 % Mg, 0.03 % Si, 0.04 % Fe, 0.25 % Ag, 0.4 % Zr, 0.01 % Zn (wt%)), were used as substrates. Before conducting the PEO process, the substrates underwent an ultrasonic bath treatment with acetone for 10 min. Subsequently, an alkaline etching in a 10 % wt./wt. NaOH solution for 30 s at 40 °C was done followed by an acid pickling in a 30 % wt./wt. HNO_3 solution at ambient temperature [48].

To produce PEO coating, a bipolar power supply from Micronics Systems was utilized to produce a square pulse pattern at a frequency of 100 Hz, a duty cycle of 30 %, and an anodic current of 5 A for 30 min.
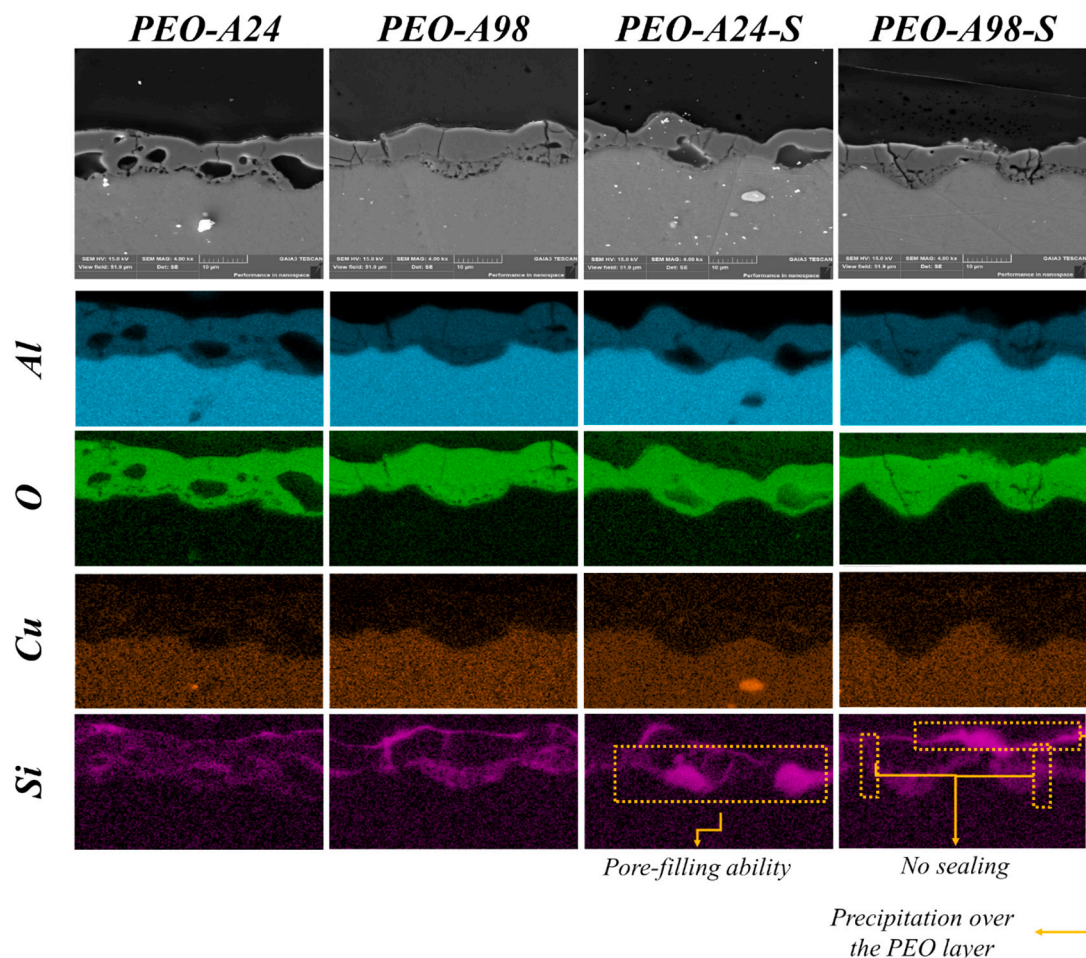
Fig. 4. Cross-sectional view as well as EDS maps of PEO coated samples before and after sol-gel sealing obtained by FE-SEM technique.

The exposed surface area was 9 cm^2, resulting in an applied current density of 0.556 A/cm^2. The proportion of positive to negative charge quantities (Q_p /Q_n) over one period of the current pulse is denoted as the RCQ parameter, adjusted at 0.9. The PEO electrolyte consisted of Na$_2$SiO$_3$ (1.65 g/L) and KOH (1 g/L), placed in a container that was attached to a cooling system in order to keep the temperature lower than 40 °C [48]. The abbreviation of PEO-A24 and PEO-A98 were employed for the PEO layer over the AA2024-T3 and AA2198-T851 substrates, respectively.

The sol-gel solution as a topcoat over the PEO samples was obtained by mixing TEOS and GPTMS sol-gel precursors with concentrations of 20 % *V*/V and 10 % V/V, respectively, for a day in a medium containing 10 % V/V ethanol as well as 60 % V/V distilled water whose pH was adjusted at 3 by acetic acid. The sol-gel layer was fabricated by dip-coating method with a 100 mm/min withdrawal rate, then cured for 1 h at 150 °C [49]. Abbreviations of PEO-A24-S and PEO-A98-S denoted PEO-A24 and PEO-A98 samples after fabrication of sol-gel coating, respectively.

The GIXRD examinations were conducted utilizing a Malvern Panalytical Empyrean X-ray diffractometer, employing θ–θ geometry and CuKα1 radiation (λ = 0.1540598 nm). Scans were captured within the range of 10° to 70°, with an incremental interval of 0.026° and a one-second duration per step. The surface topography and cross-sectional observation of the PEO-coated coupons before and after immersion in 0.1 M NaCl solution were obtained by the FE-SEM technique, utilizing a Hitachi SU5000 instrument. The porosity evaluation was performed by using *ImageJ* software, and at least two computations were performed for every sample at 100× magnification. By changing the threshold

values, the automated threshold was employed, verifying that the porosity results consistently fell within an acceptable range. After repeating measurements on several photos and computing statistical factors like standard deviation, the measurement error was determined. Roughness measurements have been achieved with a Hirox KH-8700 digital microscope (average of five measurements).

The protective properties of various PEO samples as well as sealing qualities were inspected by the EIS technique upon two-week immersion in the saline electrolyte. The standard three-electrode setup was utilized, with Ag/AgCl/KCl (+197 mV/SHE) acting as the reference electrode, platinum serving as the auxiliary electrode, and coated panels employed as working electrodes. EIS results were obtained by applying a sine wave modulation with a 10-mV peak-to-peak amplitude across the frequency domain of 100 kHz to 100 mHz. The coupons were subjected to the aggressive solution with an exposed surface area of 1.0 cm^2. To ensure the accuracy of the electrochemical measurements, each set of samples underwent a minimum of two measurements during every immersion time. In order to capture electrochemical factors relevant to the corrosion occurrence, the electrochemical findings were subjected to a curve fitting. This was accomplished by employing the most appropriate electrical equivalent circuit (EEC) within the *ZView* software.

The coefficients of friction (COFs) were measured with a Bruker UMT tribolab reciprocal sliding device. The total sliding distance (100 m) was calculated with the use of a frequency of 2 Hz, a stroke length of 10 mm, and a sliding time of 2500 s. The applied load was set at 2 N with alumina balls as counterparts. The test was reproduced for each sample three times. COFs were recorded and treated by dedicated Bruker software. After sliding tests, wear volumes were measured by Hirox KH-
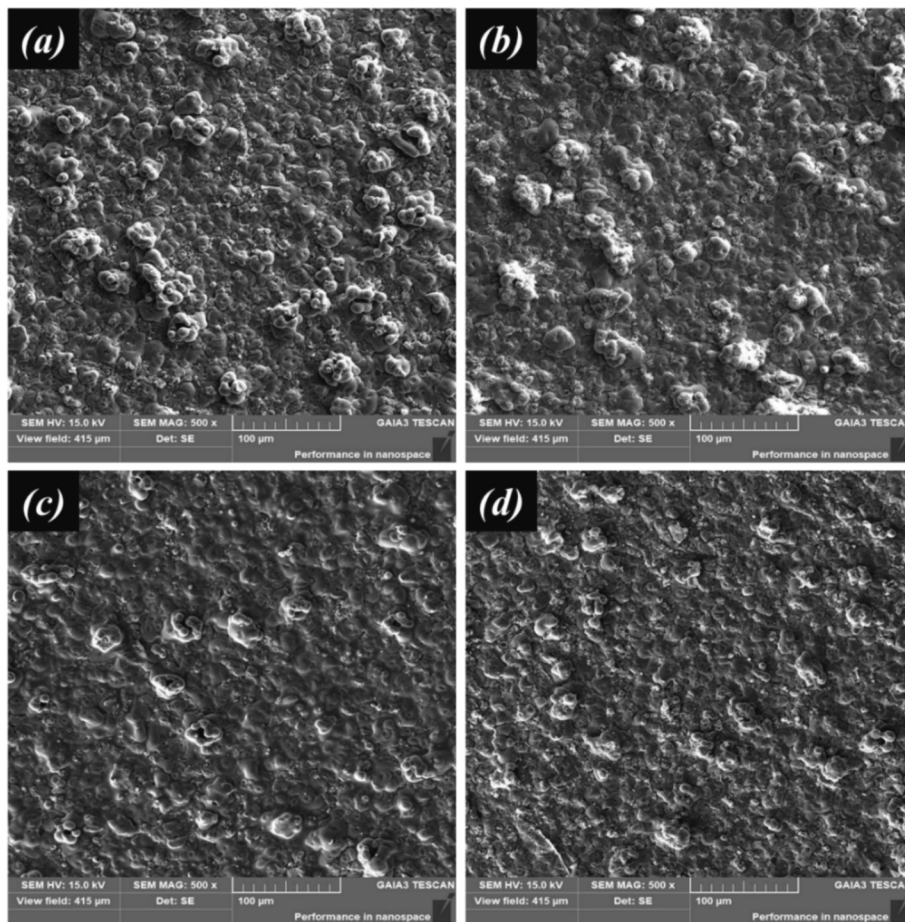
Fig. 5. Top-view observation of PEO samples related to PEO-A24(a), PEO-A98 (b), PEO-A24-S(c), and PEO-A98-S (d) after two weeks of immersion in 0.1 M NaCl electrolyte.

8700 digital microscope assuming that there is no wear on the alumina ball and by measuring the geometry of the worn tracks [50]. Wear mechanisms were characterized by FE-SEM equipped with EDS analysis.

3. Results and discussion

3.1. Average voltage-time diagram

The average voltage time response during the PEO process for AA2024-T3 and AA2198-T851 substrates is depicted in Fig. 1. Similar to other investigations [25,51], three steps are identified in both curves. During the initial phase, identical to the anodizing procedure, the average voltage exhibited a direct correlation with time, resulting in the gradual formation of a slim oxide film layer in the alkaline silicate electrolyte. In the second phase, elevating the voltage until exceeding the breakdown voltage (V_B) led to a dielectric breakdown in certain vulnerable and dispersed areas across the insulating film, accompanied by spark discharges. During the third stage, identified as the micro-discharge step, the average voltage changed at a plodding pace over time and stabilized at a constant value.

Apart from these similar stages taking place for both PEO coatings, some differences are noticed, namely the slope of region I as well as V_B. By comparison between PEO-A24 and PEO-A98, it is found that the V_B of PEO-A24 is lower than PEO-A98. Moreover, in our previous study, it was shown that the quantity and distribution of intermetallic particles in AA2024-T3 are significantly higher than in AA2198-T851. Therefore, one could expect that the higher the density of the intermetallic particles, the higher the nucleation sites for the PEO process, leading to obtaining a more porous structure in PEO-A24 than in PEO-A98. Moreno

et al. revealed that the Zn-rich intermetallic particles could affect the PEO coating morphology on magnesium alloy, forming larger voids in the vicinity of Zn-rich sites [52]. In another study committed to comprehending the impact of Cu-rich intermetallic compounds on the formation of layered double hydroxide (LDH) conversion coating, researchers found that the presence of copper-rich intermetallic particles caused the Al matrix dissolution, creating cavities/voids at their interface and matrix [53]. They pointed out that the presence of Mg makes the S-phase particles more active than the rest of the copper-based intermetallic particles; nevertheless, the nearby matrix dissolves in all intermetallic particles due to the local nano-galvanic effect. Consequently, despite the same shape of the voltage-time curves, the difference in slope in zone II can be associated with a greater amount and distribution of intermetallic particles in AA2024-T3 leading to a more porous layer. Furthermore, the presence of lithium in AA2198-T851 can contribute to the growth of oxide phases with enhanced protective properties [54], requiring a higher voltage to start stage II.

3.2. GIXRD analysis

The GIXRD outcome of the PEO layer created on AA2024-T3 and AA2198-T851 are displayed in Fig. 2. PEO coatings on aluminum alloys are often composed of α-Al_2O_3 and γ-Al_2O_3; however, amorphous alumina PEO layers have also been reported in another research [55]. Anodic oxidation and the oxide-forming process that occurs in the early stage of PEO are similar processes. When micro-arcing commences, the temperature rises rapidly due to the formation of plasma channels, triggering the primary oxide layer to transform into the metastable γ-Al_2O_3 [56]. It is interesting to note that γ-Al_2O_3 can change into
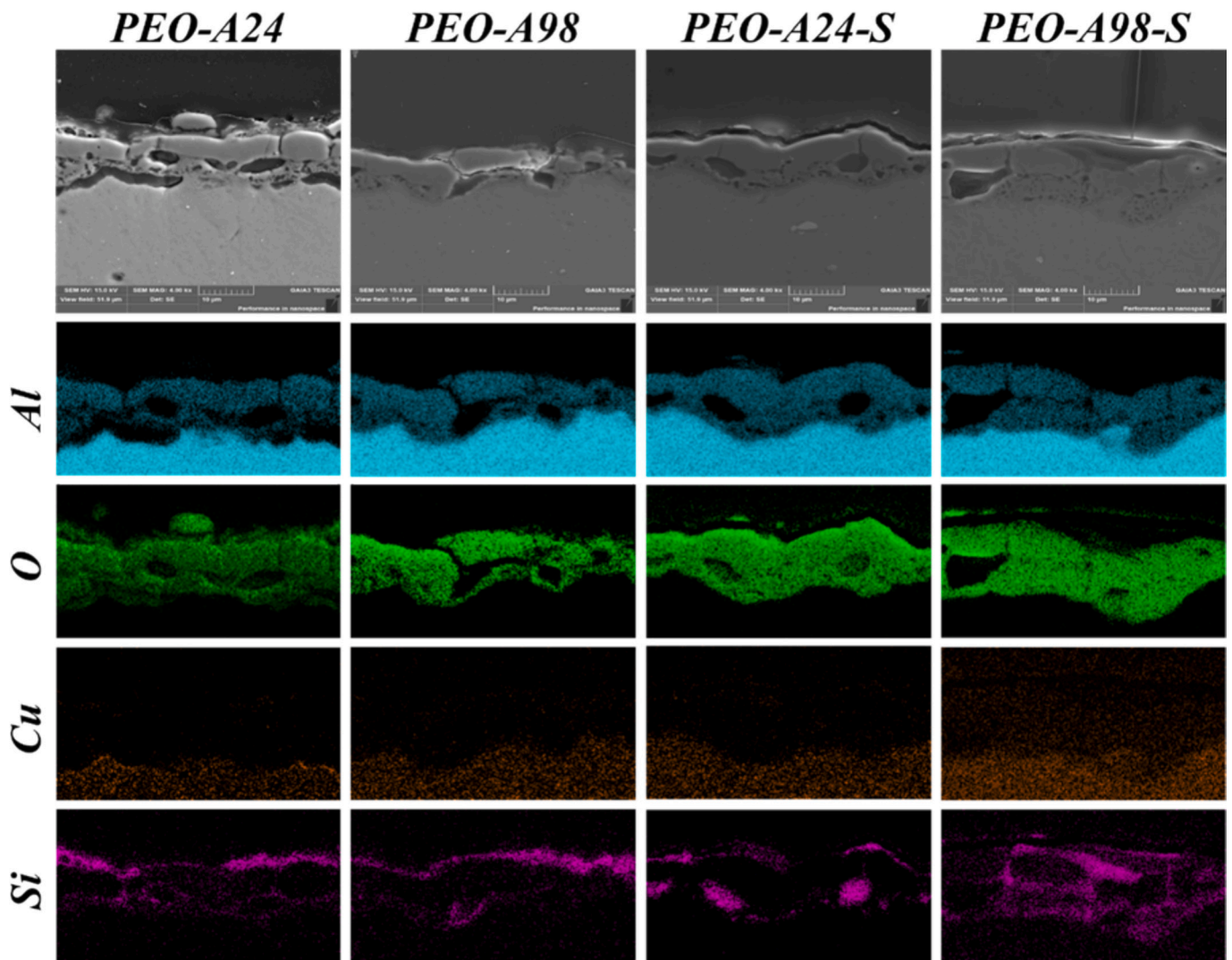
Fig. 6. Cross-sectional view as well as EDS maps of PEO coated with/without sol-gel sealing after two weeks of immersion in the saline electrolyte.

α-Al$_2$O$_3$ at higher current densities or for longer oxidation durations [57,58]. Fig. 2a and b show some intense peaks assigned to γ-Al$_2$O$_3$ as well as some shoulders related to the aluminum alloy. There is very little α-Al$_2$O$_3$ present in both PEO coatings. One possible explanation for this is that the phase transition from γ-Al$_2$O$_3$ to α-Al$_2$O$_3$ (which begins at about 1000 °C) could not be initiated by the applied current density and subsequent discharge voltage [51,59]. The GIXRD test was also carried out after the fabrication of the sol-gel coating in both PEO cases. Not much difference could be detected in the GIXRD spectra of PEO-A24 and PEO-A24-S. As it is well-documented, this type of sol-gel sealing is able to diffuse and fill the PEO pores and defects [24,42,45] on AA2024-T3. On the other hand, by comparison to the GIXRD outcome of PEO-A98 and PEO-A98-S, almost all characteristic peaks of PEO-A98 disappeared after the fabrication of the sol-gel. It is reasonable to assume that the sol-gel presents mainly over the PEO pores, forming a layer that may absorb or scatter the X-rays before reaching the PEO layer, leading to a reduced signal in the GIXRD pattern.

3.3. FE-SEM observations

3.3.1. Before immersion into the aggressive solution

The FE-SEM images in Fig. 3 depict the surface morphology and the mean porosity (denoting the proportion of the entire surface area exhibiting porosity) of the coated samples. The PEO process, conducted in a solution containing silicates, results in the formation of characteristic porous structures on aluminum alloys due to the recurrent oxide film melting and solidification. The dielectric breakdown, along with plasma reactions and scattered spark generation, leads to the formation of numerous pores and cracks scattered randomly across the surface. Comparison between the surface topography of PEO-A24 and PEO-A98 shows that the porosity of the surface is lower in PEO-A98. In other words, the surface of PEO-A98 seems to be smoother and to present smaller pores. The average diameter of pores in PEO-A24 and PEO-A98 is evaluated as 9.94 $\pm$ 1.3 μm and 6.29 $\pm$ 0.95 μm, respectively. Moreover, the average roughness (R_a) for PEO-A24 and PEO-A98 is 0.74 $\pm$ 0.15 μm and 0.44 $\pm$ 0.10 μm, respectively. In another study, it was discovered that the passive layer of the Al-Cu-Li has higher resistivity to breakdown than Al—Cu alloy, suggesting that by utilizing identical parameters, the porosity and pore diameter are comparatively lower in AA2198-T851 alloy [12]. Following the implementation of sol-gel for both PEO layers, a significant portion of the pores were successfully sealed; however, a few corresponding large ones remained visible.

Fig. 4 presents FE-SEM images and EDS maps obtained on the cross-section of the PEO coatings. In the PEO coatings, one would expect the emergence of silicon (Si), oxygen (O), and aluminum (Al) elements due to the oxidation process that occurs in the silicate solution. Notably, the PEO-A24 coating exhibits relatively larger pores, while the PEO-A98 coating displays a higher prevalence of cracks. By looking at the EDS
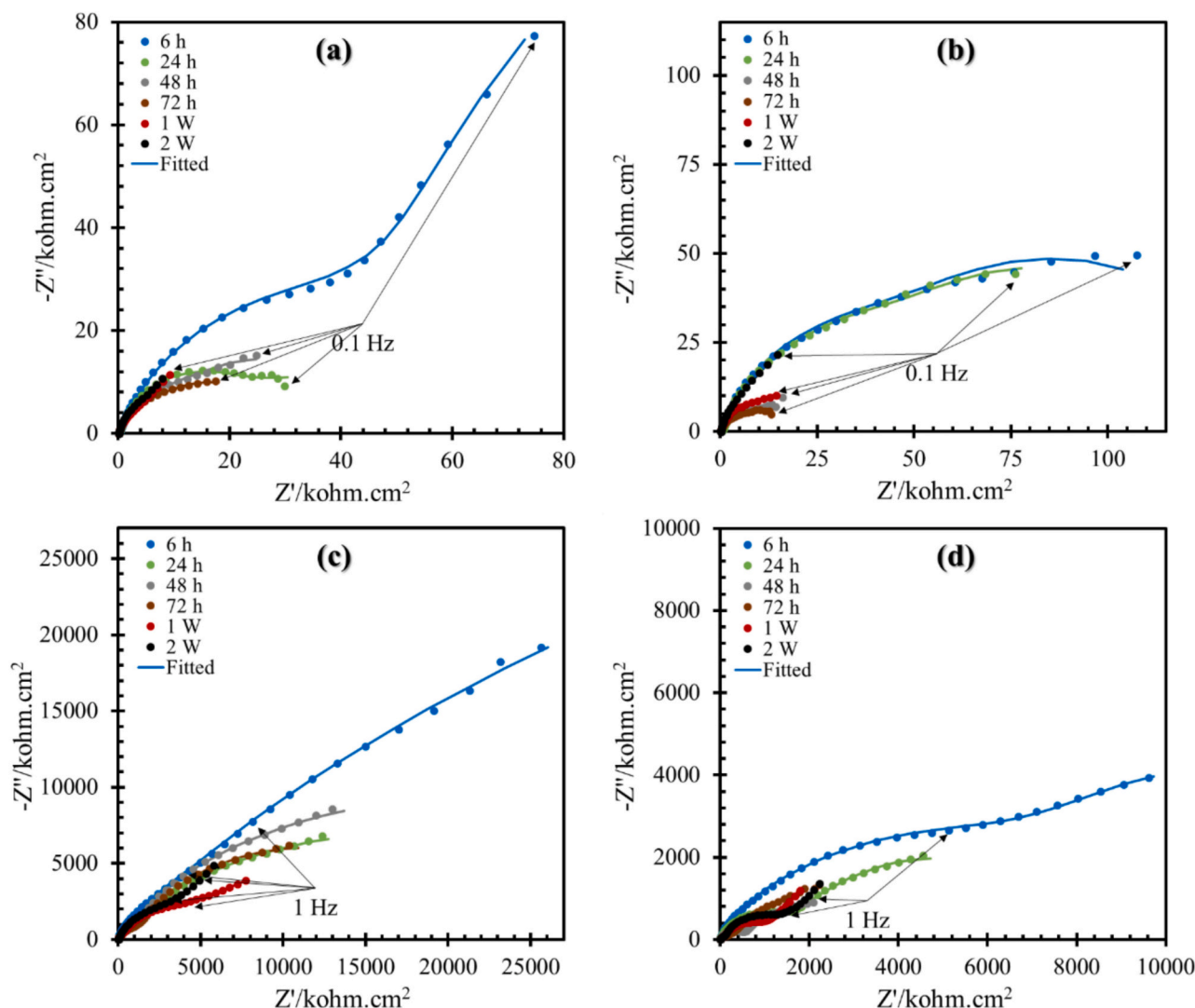
Fig. 7. Nyquist plots of PEO-coated coupons, referring to PEO-A24 (a), PEO-A98 (b), PEO-A24-S (c), and PEO-A98-S (d), for 2 weeks immersion in 0.1 M NaCl electrolyte.

maps, it could be noticed that the Si distribution in PEO-A98 is more pronounced in the crack area. It is most probably because of the fewer nucleation sites for the PEO growth and higher breakdown voltage, leading to the higher temperature at sparks. The higher temperature at sparks happening upon the PEO process resulted in the higher content of the electrolyte composition in the passive layer, particularly in the crack zone [60]. Consequently, the fewer and more intense nucleation sites facilitate the migration of Si from the electrolyte to the coating, resulting in a less homogeneous distribution of Si in the PEO-A98 coating compared to the original PEO-A98. However, it is noteworthy that the thickness of PEO-A24 and PEO-A98 is 11.94 ± 4.7 μm and 11.38 ± 4.6 μm, respectively, indicating minimal differences in their thickness. Consequently, these distinct structural morphologies result in the observation of dissimilar sol-gel sealing behaviors. In the case of PEO-A24-S, the sol-gel effectively diffuses through the pores and fills them, as visually indicated by the Si elemental map. Conversely, in the PEO-A98 coating, the sol-gel material prefers to deposit on the PEO layer instead of penetrating through it. This is likely attributed to the presence of available spaces in the PEO-A24 coating, allowing the sol-gel to pass through, whereas the presence of cracks in the PEO-A98 coating likely induces a capillary effect, causing the sol-gel to precipitate at the top surface. The Si elemental map clearly demonstrates the presence of an unsealed crack, marked in the corresponding figure, which highlights

the inadequate pore-filling ability of the sol-gel coating for PEO-A98.

3.3.2. After immersion into the aggressive solution

The planar FE-SEM images of the coupons after 14 days of dipping into the 0.1 M NaCl are presented in Fig. 5. The distinct feature of the PEO coating can still be observable, while the amount of corrosion product differs from one to another. In PEO-A24 and PEO-A98, corrosion products formed all over the surface in a way that some open pores in PEO-A24 are noticed while the corrosion products block the pores in PEO-A98. It originates from the topography of the porous layer in which PEO-A24 is accompanied by pores whereas PEO-A98 is along with cracks. After application of the sol-gel, although somehow degradation of the sol-gel layer is disclosed, the PEO-A24-S has undergone the minimum corrosion attack.

To obtain a clearer discernment of what has become of the PEO-coated samples after two weeks of immersion, the cross-sectional images and EDS maps are shown in Fig. 6. In PEO-A24 and PEO-A98, the presence of pores and cracks provide diffusion pathways for the aggressive electrolyte which is why a severe deterioration took place. A darkened area, most probably showing the delimitation of the coating from the substrate caused by the electrolyte ingress, is noticed in both unsealed PEO coatings. It is worthwhile mentioning that the morphology of PEO-A98 before the immersion contained cracks;
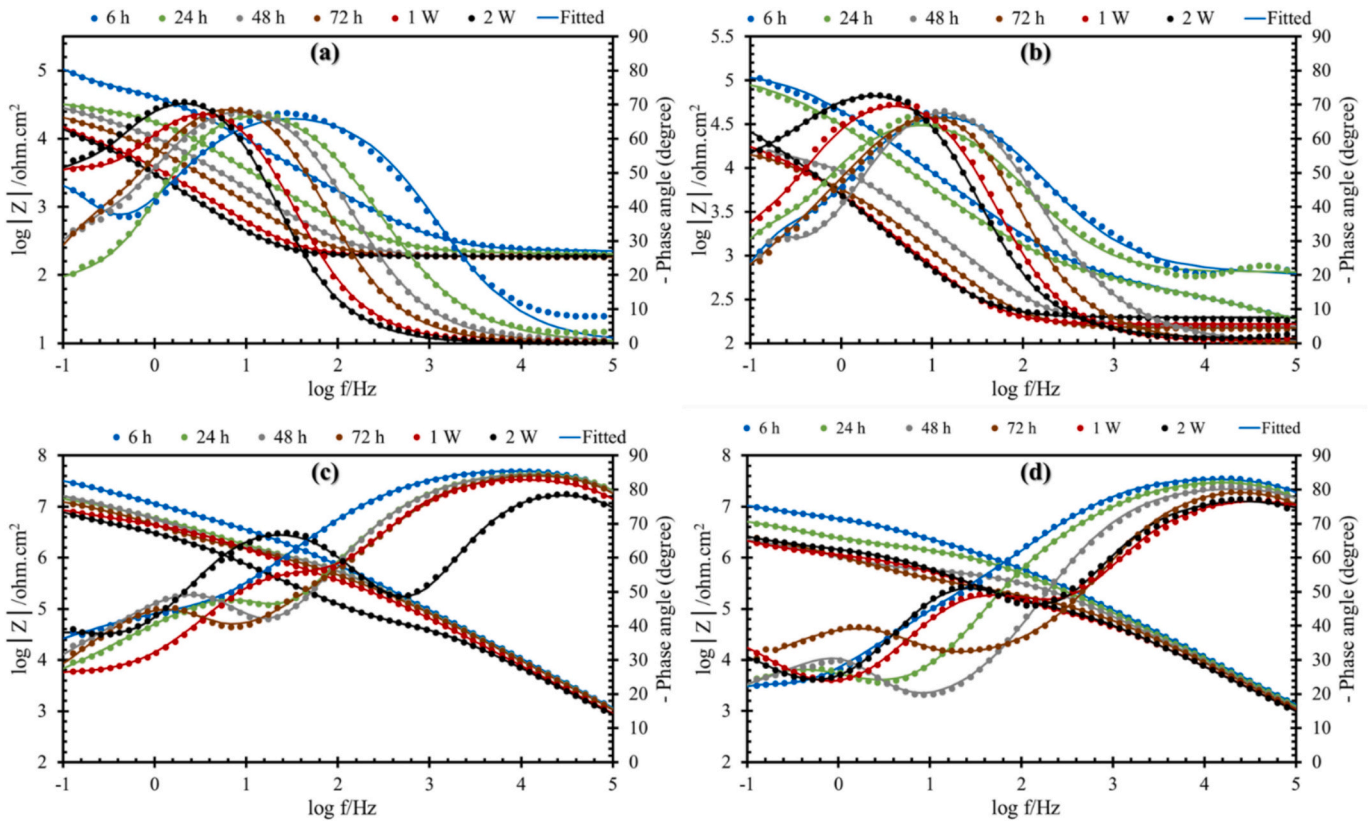
Fig. 8. Bode results of PEO-coated coupons for 2 weeks immersion in 0.1 M NaCl electrolyte, related to PEO-A24 (a), PEO-A98 (b), PEO-A24-S (c), and PEO-A98-S (d) samples.
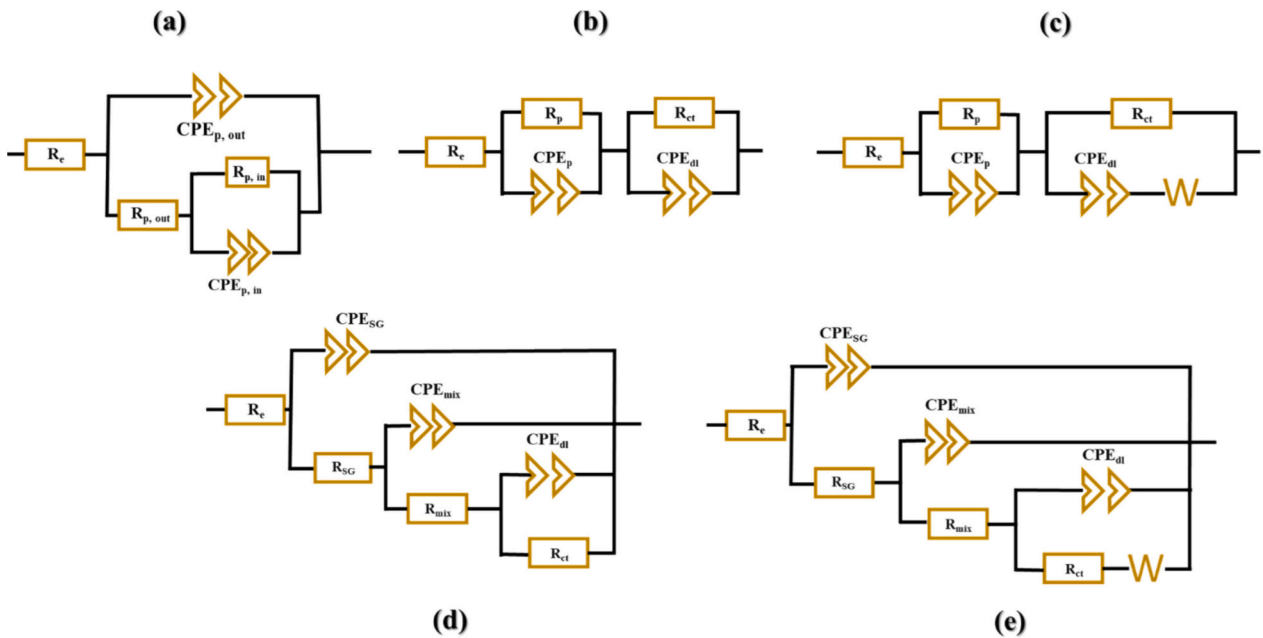

Fig. 9. Various EECs for fitting the EIS data upon immersion for two weeks in saline solution.

however, the dissolution of the substrate and corrosion reactions created some pores. The trace of the sol-gel sealing is determined by Si and O elements in the PEO-A24-S, illustrating the reliable barrier properties of the coating to sustain for two weeks in the pores. For PEO-A98-S, likewise to the images before the immersion, sol-gel remains over the PEO coating; however, the insufficient pore-filling properties caused the

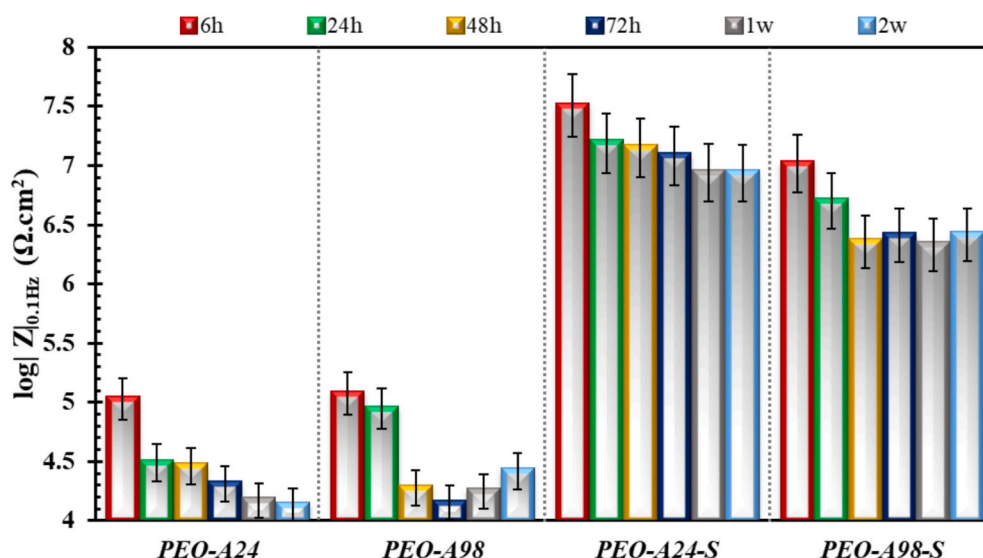diffusion of the aggressive electrolyte in which an unsealed pore suggested the dissolving of the oxide layer upon the immersion time.

In both PEO cases, a notably higher content of Si is observed on the top surface after immersion. It is worth mentioning that, prior to the exposure, a uniform distribution of Si was documented in the EDS maps. It appears that the Si within the PEO coating was directed outward from

Table 1
The summary of electrochemical parameters after fitting with different EECs.

| Sample	Immersion time in an hour (h) and week (w)	EEC	R_{SG} (kΩ cm²)	CPE_{SG}		R_{mix} or R_p (kΩ cm²)	CPE_{mix} or CPE_P		R_{ct} (kΩ cm²)	CPE_{dl}		R_W (kΩ cm²)
				Y_0 (nΩ⁻¹ cm⁻² sⁿ)	n		Y_0 (nΩ⁻¹ cm⁻² sⁿ)	n		Y_0 (nΩ⁻¹ cm⁻² sⁿ)	n	–
PEO-A24	6 h	a	–	–	–	75	3593	0.79	293.00	16,051.00	0.96	–
	24 h	b	–	–	–	36	72,787	0.64	20.00	8757.00	0.91	–
	48 h	b	–	–	–	37	49,143	0.79	10.00	21,241.00	0.90	–
	72 h	b	–	–	–	23	64,442	0.89	7.00	33,149.00	0.92	–
	1w	b	–	–	–	41	119,420	0.91	5.00	66,165.00	0.90	–
	2w	b	–	–	–	32	149,470	0.97	6.00	86,905.00	0.91	–
PEO-A98	6 h	c	–	–	–	42	3844	0.95	0.42	5200.70	0.54	98.46
	24 h	c	–	–	–	34	6930	0.96	0.46	7052.90	0.52	95.61
	48 h	c	–	–	–	8	14,032	0.95	0.03	9358.10	0.49	35.95
	72 h	c	–	–	–	3	27,592	0.98	0.07	56,303.00	0.81	14.52
	1w	c	–	–	–	6	47,954	0.95	0.09	87,412.00	0.83	23.83
	2w	c	–	–	–	10	67,396	0.97	0.20	71,382.00	0.82	119.61
PEO-A24-S	6 h	d	679.29	2.18	0.96	36,584	31.16	0.44	153,600	2.90	0.82	–
	24 h	d	312.65	2.43	0.96	2912	56.91	0.43	34,614	4.02	0.97	–
	48 h	d	294.10	2.52	0.95	2313	51.11	0.44	45,228	9.33	0.94	–
	72 h	d	276.12	2.53	0.96	4088	55.39	0.51	20,966	15.57	0.93	–
	1w	d	448.51	3.87	0.94	4412	22.75	0.74	25,744	198.94	0.52	–
	2w	d	59.61	5.04	0.92	4021	32.62	0.84	23,820	200.65	0.70	–
PEO-A98-S	6 h	d	557.22	2.64	0.94	10,820	39.31	0.51	6601	282.60	0.95	–
	24 h	d	283.45	2.90	0.94	1556	21.32	0.60	6526	202.93	0.66	–
	48 h	d	183.15	4.28	0.91	1096	415.49	0.30	7633	76.66	0.98	–
	72 h	d	99.90	4.11	0.92	1012	305.63	0.48	5627	41.26	0.89	–
	1w	e	101.31	7.89	0.88	1120	61.22	0.74	2045	879.79	0.70	8118.40
	2w	e	135.26	8.20	0.88	1456	47.88	0.79	2021	781.78	0.68	9383.60

Fig. 10. The evolution of impedance modulus at 100mHz for different samples during exposure to the aggressive electrolyte.

the substrate and subsequently accumulated over the PEO surface. To answer this matter, first look at Al reactions when it is exposed to the studied saline solution (0.1 M NaCl, pH $\approx$ 6.5) [61]:

$$Al(s) \rightarrow Al^{3+} (aq) + 3e^- \qquad (1)$$

$$Al^{3+} (aq) + 3H_2O (l) \rightarrow Al(OH)_3 (s) + 3H^+ (aq) \qquad (2)$$
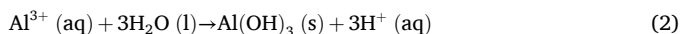
At the same time, PEO degradation occurs, resulting in the release of Si in the form of silicic acid ($Si(OH)_4$). Most probably the migration of produced silicic acid to the PEO/electrolyte interface took place, condensed, and precipitated on the PEO layer when it met the electrolyte. It probably could bring about the formation of amorphous silica particles over the PEO layer [62]. Furthermore, it could react with Al(OH)$_3$, resulting in the formation of amorphous aluminosilicate which

could also serve as a barrier layer, as illustrated by the following reaction [63,64]:

$$Al(OH)_3 (s) + Si(OH)_4 (aq) \rightarrow (HO)_2Al–O–Si (OH)_3 (s) + H_2O (l) \qquad (3)$$
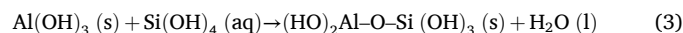
3.4. EIS assessment

The assessment of corrosion resistance for different PEO and PEO/sol-gel coatings was conducted utilizing EIS over two weeks immersed in a 0.1 M NaCl solution. The EIS data is visually represented through the Nyquist and Bode graphs in Fig. 7 and Fig. 8, respectively. Additionally, to analyze the EIS results, a set of distinct electrical equivalent circuits (EEC) is introduced in Fig. 9. The electrochemical variables, specifically R_p (PEO layer resistance), R_{SG} (sol-gel coating resistance), and R_{ct} (charge transfer resistance) were extracted and summarized in Table 1.
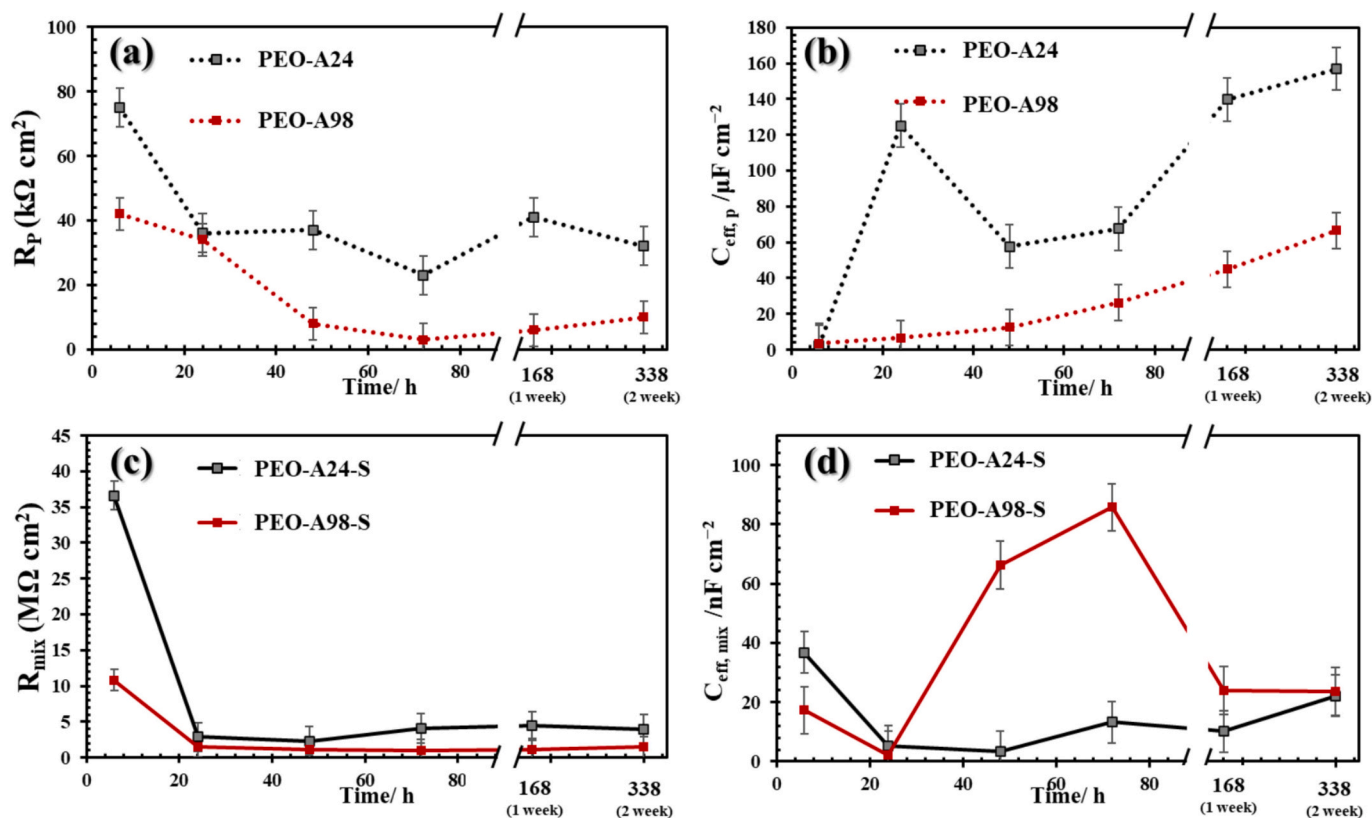
Fig. 11. The advancement of R_p and $C_{eff, p}$ for PEO-A24 and PEO-A98 (a and b) along with PEO-A24-S and PEO-A98-S (c and d), respectively.

The EIS spectra display the fitting and experimental data as solid lines and markers, respectively. Surface irregularities and non-uniformity are intrinsic characteristics of any interface, leading to the consideration of the constant phase element (CPE) rather than an ideal capacitor to interpret the EIS findings. The impedance of CPE is quantified using the formula as follows [65]:

$$Z_{CPE} = \frac{1}{Y_0 \ (i\omega)^n} \tag{4}$$

where Y_0 is the CPE admittance and n is the frequency dispersion factor, taking values between 0 and 1, signifying the shift from pure resistance to pure capacitance. The abbreviations of CPE_{dl}, CPE_p, CPE_{SG}, and CPE_{mix} (also R_{mix}) are attributed to the presence of double-layer, PEO layer, sol-gel coating, and the PEO/sol-gel mixed region, respectively. Two distinguishing layers (inner and outer layers) generally define the PEO process [66]. Since the porous layer provides diffusion routes for the corrosive medium to reach the substrate, its presence is considered a shortcoming for long-term performance.

For the PEO-A24, these two layers could be differentiated after 6 h immersion as the inner layer resistance is significantly higher than outer resistance (R_{ct} and R_p after 6 h referred to the resistance of inner and outer layers), indicating that the dense inner layer is primarily accountable for the short-term protection [67]. The degradation of the coating initiates after 24 h, which is why the time constants were adjusted to take into account both the substrate reaction and the whole coating (both inner and porous layers). Actually, some pores extended or developed, opening up routes for the corrosive medium to diffuse [68]. As a result, the utilized EEC was modified from Fig. 9a to b. The PEO layer is represented by R_p and CPE_p, while the substrate response is denoted by CPE_{dl} and R_{ct}, according to the EEC in Fig. 9b. This indicates that certain holes that are deep enough to reach the substrate developed as a result of a decrease in barrier properties after 24 h of immersion. After that, the PEO-A24 sample continues to display this electrochemical

activity for the full two-week immersion period.

For the PEO-A98 sample exposed for two weeks in the aggressive electrolyte, a dissimilar kind of electrochemical activity was found based on the employed EEC (Fig. 9c). As it was visualized by the FE-SEM images, the morphology of PEO-A98 is along with more cracks and less porosity as compared to the PEO-A24, leading to the diffusion control of aggressive elements ingress. This hypothesis was validated by the employed EEC in which the Warburg element denotes that the redox reactions are limited by diffusion of aggressive ions or oxygen [69]. The distinct structure of PEO-A98 made it have better barrier performance than PEO-A24 in short immersion (after one day); however, the corrosion resistance properties dropped from then on along with some flaws and cracks. Following the sol-gel coating application, even though an increment in corrosion resistance took place for both PEO-A24 and PEO-A98, different protection performance was noticed.

For the PEO-A24-S, the distinctive EEC (Fig. 9d) revealed that the sol-gel coating was predominant at high frequencies, while the intermediate frequency response indicated a coexistence of the PEO and sol-gel layers. Notably, the formation of R_{SG} was observed, determining the effective permeation of sol-gel into the porous PEO layer when comparing the R_{mix} and R_p amounts in the PEO-A24-S sample. However, it is noteworthy that the gradual decrease of R_{SG} and the consequent increase in the admittance element of CPE_{SG} signify a degradation in the protection qualities of the sol-gel layer when exposed to the aggressive electrolyte.

Interestingly the same type of sol-gel coating exhibited dissimilar protection performance in the PEO-A98-S sample. Despite employing an identical EEC model for fitting experimental data during 72 h of exposure to the aggressive electrolyte, the corrosion protection characteristics were notably weaker in PEO-A98-S than in PEO-A24-S. After one week of immersion, the utilized EEC switched from Fig. 9d to Fig. 9e, indicative of a shift towards diffusion-controlled redox reactions. As was demonstrated in the cross-section images, the sol-gel intended to
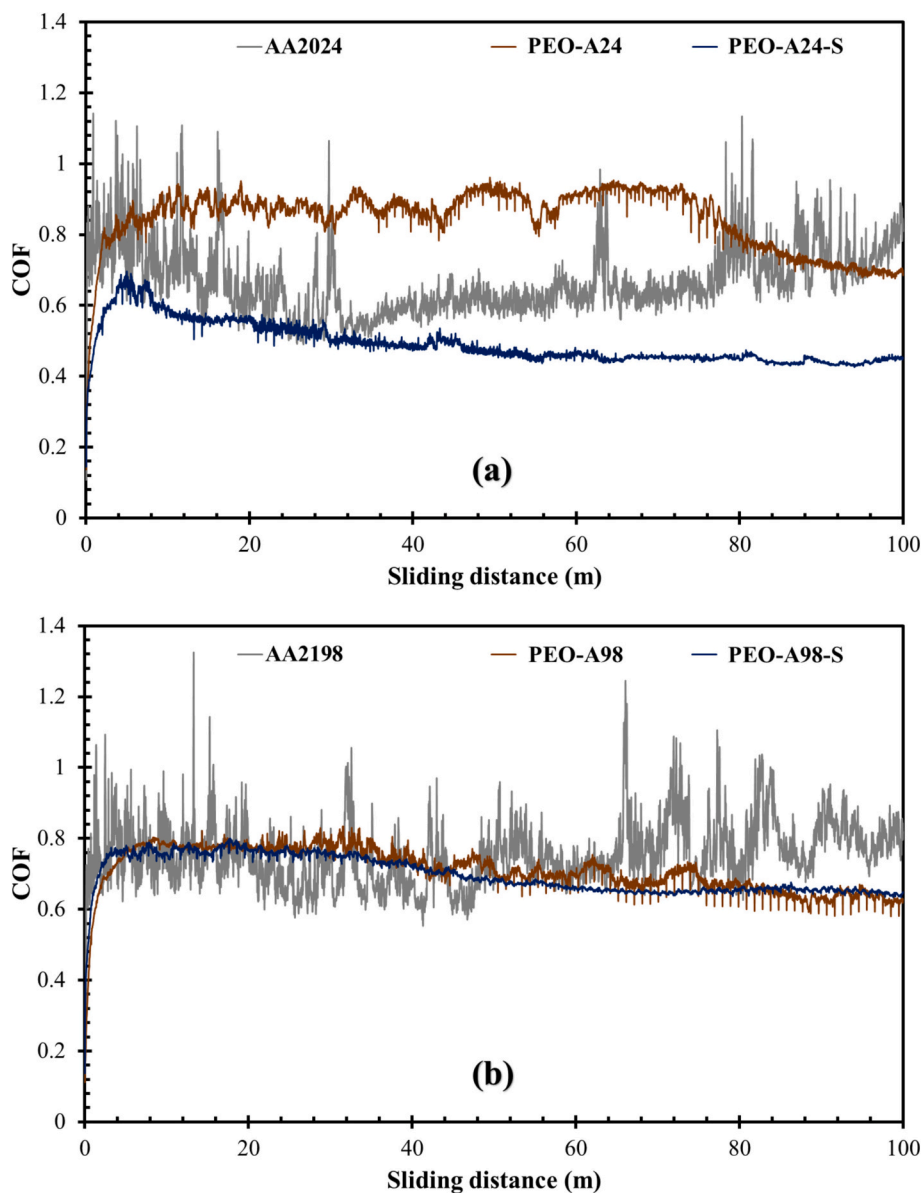
Fig. 12. COF as a function of the total sliding distance for AA2024-T3, PEO-A24, and PEO-A24-S(a) as well as AA2198-T851, PEO-A98, and PEO-A98-S (b).

precipitate dominantly over the PEO-A98 layer rather than pore-filling, forming a barrier layer against the ingress of aggressive elements into the PEO-A98 flaws. Upon immersion, the protective features of the sol-gel decreased little by little so that like what was reported for the PEO-A98, most probably the penetration of oxygen and ions was limited by diffusion control phenomenon.

The impedance modulus at low frequency of each sample during the entire immersion period was compared and exhibited in Fig. 10. The first impression could be the higher values of both PEO coatings after application of the sol-gel, no matter whether the sol-gel acts as pore-filling or layer formation over the PEO porous layer. By comparing PEO-A24 and PEO-A98 it could be noticed that in the short immersion time (up to one day), PEO-A98 had higher corrosion resistance properties than PEO-A24; however, its properties dropped significantly from then on and were lower than PEO-A24 up to 72 h immersion time. It most probably stands to reason that the distinct morphology of PEO-A98, in the beginning, hindered the diffusion of aggressive elements more than PEO-A24, but the electrolyte found pathways to access the substrate. This explanation could also be validated by the values of R_p, R_{ct}, and R_w summarized in Table 1. After 72 h of immersion, the

corrosion protection of PEO-A98 enhanced gradually and continued the increasing trend till the end of the exposure. In fact, the linear increase in impedance and the noticeable time constant at the lowest frequencies after one and two weeks of immersion were likely brought on by the corrosion product creation, leading to the blocking of pathways and diffusion routes [70]. Following the sol-gel application, the low-frequency impedance indicated a higher corrosion resistance of PEO-A24-S than PEO-A98-S in every single immersion time. As pore-filling is the main corrosion protection mechanism in PS, the emergence of the sol-gel is like cement inside the pores, hindering the diffusion of the electrolyte. While the sol-gel was not able to penetrate through the PEO-A98 pores to fill, it only created a layer over the pores so that a sort of free volumetric region exists behind the sol-gel. It is why after one week of immersion, the Warburg element appeared, illustrating that the performance qualities of the sol-gel layer declined, and the aggressive electrolyte must undergo diffusion control to reach the substrate. This hypothesis can also be confirmed by having the lowest values for R_{SG} and R_{mix} after 72 h of immersion. Moreover, some ups and downs in the PEO-A98-S sample which are most probably due to the corrosion product formation align with the hypothesis [71].
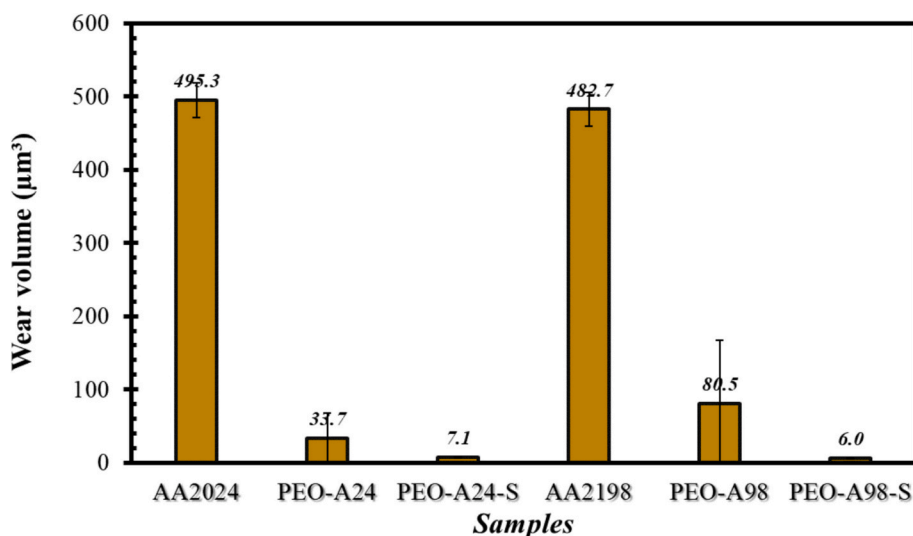
Fig. 13. Average wear volumes of the different coupons.

To get a better comparison between PEO-A24 and PEO-A98 with/without sol-gel sealing, Fig. 11 reported the advancement of R_p, R_{mix}, $C_{eff, p}$, and $C_{eff, mix}$ upon two weeks of exposure time. The following equation was used to determine the effective capacitance [72]:

$$C_{mix} = Y_{0,mix}^{1/n} R_{mix}^{(1-n)/n} \qquad (5)$$

Fig. 11a demonstrated that the protective qualities of only the PEO layer (not the whole coating plus substrate response) in PEO-A24 are higher than in PEO-A98. It is worthwhile to mention that the low-frequency impedance stated the superior properties of PEO-A98 at 24 h immersion time for instance while its R_p value is lower than PEO-A24. In Fig. 11b, the effective capacitance of PEO-A98 is lower than PEO-A24. Considering that the thickness of PEO coatings is nearly comparable, it is important to note that the higher the effective capacitance, the greater the permittivity of the coating. This increase in permittivity is attributed to water ingress into the coating. So, one could include that the water ingress in PEO-A98 was lower than PEO-A24 even though its R_p was lower. Larger holes in the PEO-A24 allow for regulated water diffusion which may have an impact on its capacitance and dielectric characteristics, while PEO-A98 on the other hand, could have a lower capacitance because of its diffusion-controlled behavior that prevents the ingress of water.

After application of the sol-gel, as it was mentioned earlier about the pore-filling ability in PEO-A24-S, the R_{mix} value of PEO-A24-S is higher than PEO-A98-S, illustrating the better sealing ability of the sol-gel for PEO-A24-S. As was depicted in the cross-section observation, the sol-gel could not penetrate the PEO-A98 cracks, making some available areas for water diffusion. Accordingly, the effective capacitance went up to 72 h of immersion because of the electrolyte diffusion followed by decrement due to diffusion-controlled behavior along with corrosion product formation.

3.5. Mechanical examination

The friction coefficients of the different coatings were compared to those of the substrates (Fig. 12). COFs of both substrates are noisy due to the roughness of the aluminum. However, the average coefficients of friction are quite stable with the sliding distance between 0.6 and 0.8. AA2024-T3 with PEO coating (PEO-A24) shows higher COF until 80 m of analysis before a decrease to a value of 0.7. On the other hand, the COF of the AA2198-T851 with PEO (PEO-A98) is more constant with the sliding distance. The difference between both parts is related to the surface roughness of the coating and the pore size distribution: as the

average roughness of the PEO-A24 is higher than the PEO-A98, the COF is higher. Indeed, longer distances are needed to eliminate the surface roughness. Fig. 12a shows a decrease in the COF of part PEO-A24 after 70 m of analysis, meaning that the roughness has been eliminated and the tribology measurement is going into steady-state conditions. In addition, larger pores imply an increase in COF due to the formation of a virtual roughness (given by the pore size distribution and not by the surface texture of the parts). The substrates were reached once for PEO-A24 and twice for PEO-A98, meaning that the chosen sliding parameters could be sufficient to remove entirely the PEO coating. After the application of sol-gel, both substrates exhibit excellent wear resistance, with low COF, around 0.5 for PS and 0.6 for PEO-A98-S. Two different behaviors are observed between PEO-A24-S and PEO-A98-S. Pores were sealed by the sol-gel; however, the sol-gel deposited over the PEO-A98 and could not sufficiently seal it. Eventually, the COF became lower in PEO-A24-S than PEO-A24 (following the sol-gel fabrication over the PEO-A24), while it remained almost unchanged in PEO-A98 once sol-gel was applied (PEO-A98-S). The wear of the parts is thus sensible to the pores, which act as defects against wear resistance.

The wear volumes are depicted in Fig. 13. The two substrates without any coating show important wear volumes of around 500 μm^3 of matter that is eliminated by the sliding test. As mentioned before, the use of a PEO coating improves the wear properties, but the results are scattered due to the presence of pores on the surface coating. Standard deviations are thus important since the aluminum substrates were reached for some of the experiments, which induced higher wear. The use of a sol-gel provides low wear volumes (5 to 8 μm^3). The substrates were not reached, meaning that the sealing with sol-gel is effective for wear protection.

FE-SEM images of the worn tracks for substrate AA2024-T3 (Fig. 14a_1 and a_2) and substrate AA2198-T851 (Fig. 14b) show grooves and scratches, meaning that abrasion is one of the main wear mechanisms. The results are consistent with those of Javidi and Fadaee [73] and Rahmati et al. [74]. The number of debris is important in the tracks. Their chemical composition shows high oxygen content (> 20 wt %), meaning that oxidation occurred during the tribology test. In the abrasion grooves, the oxygen content is lower. In Fig. 14a_2, small cracks are observed perpendicular to the sliding direction, meaning that delamination occurred for AA2024-T3 [75]. The analysis of the alumina counter bodies shows adhesion of the aluminum substrates thanks to the detection of copper and magnesium on the surface of the balls. The wear mechanism is thus a combination of abrasion, adhesion, oxidation, and delamination.

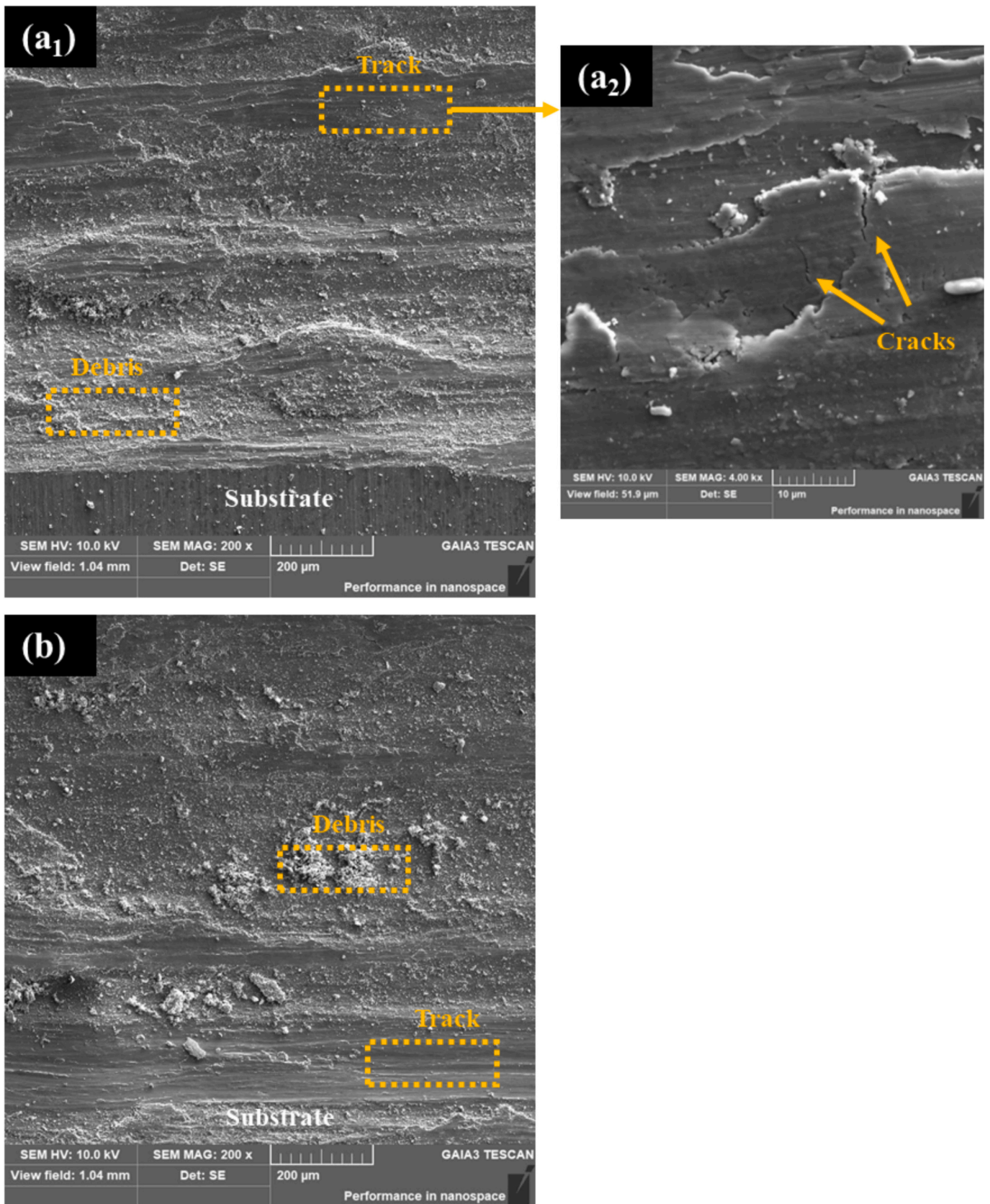Fig. 15 shows the worn tracks after the dry sliding test for PEO and

Fig. 14. FE-SEM images of the worn tracks (center of the track) after dry sliding test for AA2024-T3 in two magnifications (a_1 and a_2) and AA2198-T851 (b) substrates.
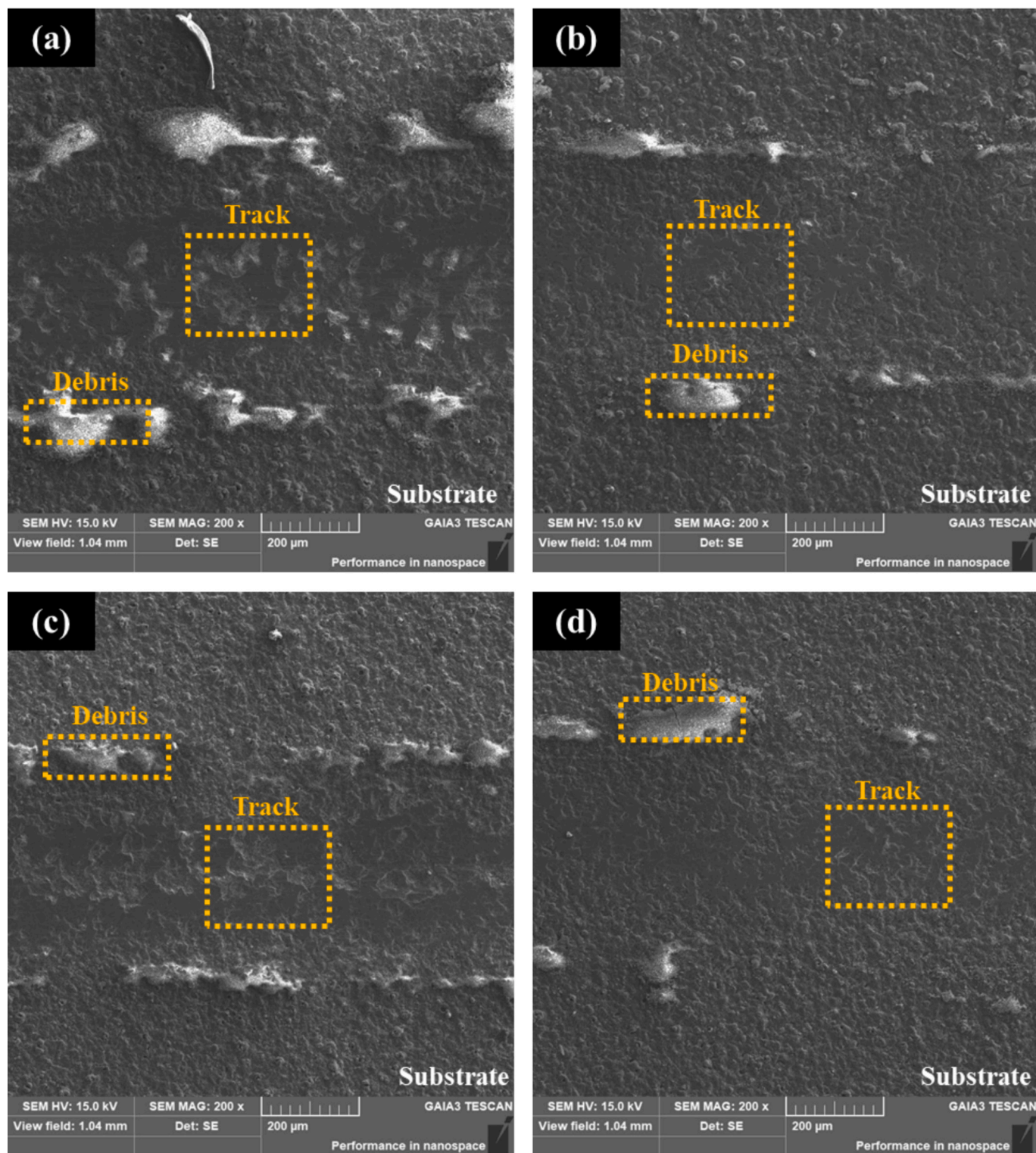
Fig. 15. FE-SEM images of the worn tracks (center of the track) after the dry sliding test for the parts exhibiting coating: PEO-A24 (a), PEO-A24-S (b), PEO-A98 (c), and PEO-A98-S (d).

PEO/sol-gel coating on both aluminum substrates. Very few grooves parallel to the sliding direction are observed on the four parts, meaning that abrasion is not the main wear mechanism. Flattening of the surface (elimination of the surface roughness) and delamination areas are observed on the worn tracks [48,73]. The debris is of the same composition as the PEO coating and is thus matter that has been pulled out of the track. The third body rolling mechanism is responsible for the

production of the debris [76]. However, those results must be taken with care since some of the experiments have shown that the PEO coatings were removed during the tribotest (PEO-A24 and PEO-A98 parts). One explanation could be the tendency of the PEO coating to crack with the action of the ambient humidity. If cracks are present at the surface the resistance of the coating against wear is reduced. The counter alumina balls show some adhesion on their surface with the presence of Cu, Si,

and Mg for PEO coatings (PEO-A24 and PEO-A98 parts). The PEO/sol-gel shows high wear resistance with only flattening of the surface and pulling out of the debris outside the track. The use of sol-gel inhibits the cracking of the PEO coating due to the humidity. Moreover, the counter alumina balls show only limited Si content (< 2 wt%) on their surface, meaning that some adhesion occurred. Similar results have been observed by Khalid et al. [21] on sol-gel sealed PEO coating on AA2024-T3.

4. Conclusion

- PEO coatings were created on AA2024-T3 and AA2198-T851 substrates using identical conditions, including electrolyte composition and electrical parameters. Both coatings exhibited inherent porous structures; thus, a sol-gel layer was synthesized and applied to enhance their electrochemical and wear properties.
- Due to the different chemical compositions and microstructures of the two aluminum alloys, the resulting PEO coatings had distinct morphologies, leading to differences in sol-gel sealing, wear properties, and corrosion resistance.
- The PEO coating on AA2024-T3 exhibited more porosity compared to AA2198-T851; however, AA2198-T851 showed more cracks. FE-SEM images revealed that the sol-gel top-coat filled the porous structure of PEO-A24, whereas mainly precipitation was observed on PEO-A98.
- EIS results indicated superior short-term corrosion behavior for PEO-A98 compared to PEO-A24; however, after sol-gel sealing, PEO-A24-S demonstrated higher protective performance due to better sealing.
- Sol-gel sealing significantly improved the performance of both PEO coatings, as confirmed by the wear test results. The wear evaluation aligned with the corrosion tests, showing a lower COF for PEO-A24-S compared to PEO-A98-S, attributed to the different sealing characteristics of the sol-gel.

CRediT authorship contribution statement

Sajjad Akbarzadeh: Writing – review & editing, Writing – original draft, Validation, Methodology, Investigation. **Rafael Emil Klumpp:** Writing – review & editing, Validation, Methodology, Investigation. **Alexandre Mégret:** Writing – original draft, Methodology, Investigation. **Vedi Ölmez:** Methodology. **Véronique Vitry:** Writing – review & editing, Funding acquisition. **Marie-Georges Olivier:** Writing – review & editing, Validation, Supervision, Methodology, Funding acquisition, Conceptualization.

Declaration of competing interest

The authors declare the following financial interests/personal relationships which may be considered as potential competing interests: Sajjad Akbarzadeh reports financial support was provided by Fédération Wallonie-Bruxelles (Actions de Recherche Concertées ARC SEALCERA). Rafael E. Klumpp reports financial support was provided by National Council for Scientific and Technological Development. If there are other authors, they declare that they have no known competing financial interests or personal relationships that could have appeared to influence the work reported in this paper.

Acknowledgments

Appendix A. Supplementary data

Supplementary data to this article can be found online at https://doi.org/10.1016/j.surfcoat.2024.131510.

Data availability

Data will be made available on request.

References

[1] M. Mokaddem, P. Volovitch, F. Rechou, R. Oltra, K. Ogle, The anodic and cathodic dissolution of Al and Al–cu–mg alloy, Electrochim. Acta 55 (2010) 3779–3786.

[2] D. Zhao, J. Sun, L. Zhang, Y. Tan, J. Li, Corrosion behavior of rare earth cerium based conversion coating on aluminum alloy, J. Rare Earths 28 (2010) 371–374.

[3] F.M. Queiroz, A.F.S. Bugarin, N.P. Hammel, V.R. Capelossi, M. Terada, I. Costa, EIS behavior of anodized and primer coated AA2198–T3 compared to AA2024–T3 exposed to salt spray CASS test, Surf. Interface Anal. 48 (2016) 755–766.

[4] M.K. Cavanaugh, J.-C. Li, N. Birbilis, R.G. Buchheit, Electrochemical characterization of intermetallic phases common to aluminum alloys as a function of solution temperature, J. Electrochem. Soc. 161 (2014) C535–C543.

[5] F.M. Queiroz, M. Magnani, I. Costa, H.G. de Melo, Investigation of the corrosion behaviour of AA 2024-T3 in low concentrated chloride media, Corros. Sci. 50 (2008) 2646–2657.

[6] L. Lacroix, C. Blanc, N. Pébère, G.E. Thompson, B. Tribollet, V. Vivier, Simulating the galvanic coupling between S-Al2CuMg phase particles and the matrix of 2024 aerospace aluminium alloy, Corros. Sci. 64 (2012) 213–221.

[7] J. Vander Kloet, A.W. Hassel, M. Stratmann, Effect of pretreatment on the intermetallics in aluminum alloy 2024-T3, Zeitschrift Fur Phys, Chemie 219 (2005) 1505–1518.

[8] R.J. Rioja, J. Liu, The evolution of Al-Li base products for aerospace and space applications, Metall. Mater. Trans. A Phys. Metall. Mater. Sci. 43 (2012) 3325–3337.

[9] N. Eswara Prasad, A.A. Gokhale, P. Rama Rao, Mechanical behaviour of aluminium-lithium alloys, Sadhana - Acad, Proc. Eng. Sci. 28 (2003) 209–246.

[10] U. Donatus, M. Terada, C.R. Ospina, F.M. Queiroz, A. Fatima Santos Bugarin, I. Costa, On the AA2198-T851 alloy microstructure and its correlation with localized corrosion behaviour, Corros. Sci. 131 (2018) 300–309.

[11] D. Georgoulis, C.M. Charalampidou, N. Siskou, N.D. Alexopoulos, S.K. Kourkoulis, Corrosion behaviour of AA2198–T8 and AA2024–T3 alloy in 3.5% aqueous solution, Procedia Struct. Integr. 28 (2020) 2297–2303.

[12] M.X. Milagre, U. Donatus, C.S.C. Machado, J.V.S. Araujo, R.M.P. da Silva, B.V.G. de Viveiros, A. Astarita, I. Costa, Comparison of the corrosion resistance of an Al–cu alloy and an Al–cu–Li alloy, Corros. Eng. Sci. Technol. 54 (2019) 402–412.

[13] K.A. Yasakau, J. Tedim, M.L. Zheludkevich, M.G.S. Ferreira, Smart self-healing coatings for corrosion protection of aluminium alloys, Handb. Smart Coatings Mater. Prot. (2014) 224–274.

[14] X. Verdalet-Guardiola, B. Fori, J.P. Bonino, S. Duluard, C. Blanc, Nucleation and growth mechanisms of trivalent chromium conversion coatings on 2024-T3 aluminium alloy, Corros. Sci. 155 (2019) 109–120.

[15] F. Yu, L. Camilli, T. Wang, D.M.A. Mackenzie, M. Curioni, R. Akid, P. Bøggild, Complete long-term corrosion protection with chemical vapor deposited graphene, Carbon N. Y. 132 (2018) 78–84.

[16] G.M. Rao, A.V. Dilkush, Gopal, effect of physical vapour deposition coated and uncoated carbide tools in turning aluminium alloy-AA6063, Mater. Today Proc. 41 (2021) 1212–1219.

[17] C. Haixiang, K. Dejun, Comparison on electrochemical corrosion performances of arc and laser thermal sprayed Al–Ti–Ni coatings in marine environment, Mater. Chem. Phys. 251 (2020) 123200.

[18] A.I. Ryabchikov, E.B. Kashkarov, A.E. Shevelev, A. Obrosov, D.O. Sivin, Surface modification of Al by high-intensity low-energy Ti-ion implantation: microstructure, mechanical and tribological properties, Surf. Coat. Technol. 372 (2019) 1–8.

[19] L.F. Wang, J. Sun, X.L. Yu, Y. Shi, X.G. Zhu, L.Y. Cheng, H.H. Liang, B. Yan, L. J. Guo, Enhancement in mechanical properties of selectively laser-melted AlSi10Mg aluminum alloys by T6-like heat treatment, Mater. Sci. Eng. A 734 (2018) 299–310.

[20] V.R. Capelossi, M. Poelman, I. Recloux, R.P.B. Hernandez, H.G. De Melo, M. G. Olivier, Corrosion protection of clad 2024 Aluminum alloy anodized in tartaric-sulfuric acid bath and protected with hybrid sol–gel coating, Electrochim. Acta 124 (2014) 69–79.

[21] H.A. Khalid, S. Akbarzadeh, Y. Paint, V. Vitry, M.G. Olivier, Comparison of Tribological characteristics of AA2024 coated by plasma electrolytic oxidation (PEO) sealed by different sol–gel layers, Coatings 13 (2023) 871.

[22] R. del Olmo, M. Mohedano, P. Visser, E. Matykina, R. Arrabal, Flash-PEO coatings loaded with corrosion inhibitors on AA2024, Surf. Coat. Technol. 402 (2020) 126317.

[23] R. Arrabal, M. Mohedano, E. Matykina, A. Pardo, B. Mingo, M.C. Merino, Characterization and wear behaviour of PEO coatings on 6082-T6 aluminium alloy with incorporated α-Al2O3 particles, Surf. Coat. Technol. 269 (2015) 64–73.

[24] S. Akbarzadeh, L. Sopchenski Santos, V. Vitry, Y. Paint, M.G. Olivier, Improvement of the corrosion performance of AA2024 alloy by a duplex PEO/clay modified sol-gel nanocomposite coating, Surf. Coat. Technol. 434 (2022) 128168.

[25] B. Mingo, Y. Guo, A. Němcová, A. Gholinia, M. Mohedano, M. Sun, A. Matthews, A. Yerokhin, Incorporation of halloysite nanotubes into forsterite surface layer during plasma electrolytic oxidation of AM50 mg alloy, Electrochim. Acta 299 (2019) 772–788.

[26] P. Molaeipour, S.R. Allahkaram, S. Akbarzadeh, Corrosion inhibition of Ti6Al4V alloy by a protective plasma electrolytic oxidation coating modified with boron carbide nanoparticles, Surf. Coat. Technol. 430 (2022) 127987.

[27] K. Li, W. Li, G. Zhang, W. Zhu, F. Zheng, D. Zhang, M. Wang, Effects of Si phase refinement on the plasma electrolytic oxidation of eutectic Al-Si alloy, J. Alloys Compd. 790 (2019) 650–656.

[28] H. jun XIE, Y. liang CHENG, S. xian LI, J. hui CAO, L. CAO, Wear and corrosion resistant coatings on surface of cast A356 aluminum alloy by plasma electrolytic oxidation in moderately concentrated aluminate electrolytes, Trans. Nonferrous Met. Soc. China 27 (2017) 336–351.

[29] L. Wang, L. Chen, Z. Yan, W. Fu, Optical emission spectroscopy studies of discharge mechanism and plasma characteristics during plasma electrolytic oxidation of magnesium in different electrolytes, Surf. Coat. Technol. 205 (2010) 1651–1658.

[30] L.O. Snizhko, A.L. Yerokhin, A. Pilkington, N.L. Gurevina, D.O. Misnyankin, A. Leyland, A. Matthews, Anodic processes in plasma electrolytic oxidation of aluminium in alkaline solutions, Electrochim. Acta 49 (2004) 2085–2095.

[31] M. Treviño, R.D. Mercado-Solis, R. Colás, A. Pérez, J. Talamantes, A. Velasco, Erosive wear of plasma electrolytic oxidation layers on aluminium alloy 6061, Wear 301 (2013) 434–441.

[32] J. Joo, D. Kim, H.S. Moon, K. Kim, J. Lee, Durable anti-corrosive oil-impregnated porous surface of magnesium alloy by plasma electrolytic oxidation with hydrothermal treatment, Appl. Surf. Sci. 509 (2020) 145361.

[33] D.V. Mashtalyar, K.V. Nadaraia, I.M. Imshinetskiy, E.A. Belov, V.S. Filonina, S. N. Suchkov, S.L. Sinebryukhov, S.V. Gnedenkov, Composite coatings formed on Ti by PEO and fluoropolymer treatment, Appl. Surf. Sci. 536 (2021) 147976.

[34] L. Pezzato, R. Babbolin, P. Cerchier, M. Marigo, P. Dolcet, M. Dabalà, K. Brunelli, Sealing of PEO coated AZ91magnesium alloy using solutions containing neodymium, Corros. Sci. 173 (2020) 108741.

[35] S. Akbarzadeh, R. Naderi, M. Mahdavian, Fabrication of a highly protective silane composite coating with limited water uptake utilizing functionalized carbon nanotubes, Compos. Part B Eng. 175 (2019) 107109.

[36] S. Akbarzadeh, K. Akbarzadeh, M. Ramezanzadeh, R. Naderi, M. Mahdavian, M. G. Olivier, Corrosion resistance enhancement of a sol-gel coating by incorporation of modified carbon nanotubes: artificial neural network (ANN) modeling and experimental explorations, Prog. Org. Coat. 174 (2023) 107296.

[37] J.D. Mackenzie, E.P. Bescher, Physical properties of sol-gel coatings, J. Sol-Gel Sci. Technol. 19 (2000) 23–29.

[38] A. Mehner, H.W. Zoch, W. Datchary, G. Pongs, Sol-gel coatings for high precision optical molds, CIRP Ann. 55 (2006) 589–592.

[39] S. Akbarzadeh, M. Ramezanzadeh, M. Ramezanzadeh, M. Mahdavian, R. Naderi, Fabrication of highly effective polyaniline grafted carbon nanotubes to induce active protective functioning in a Silane coating, Ind. Eng. Chem. Res. 58 (2019) 20309–20322.

[40] D. Balgude, A. Sabnis, Sol-gel derived hybrid coatings as an environment friendly surface treatment for corrosion protection of metals and their alloys, J. Sol-Gel Sci. Technol. 64 (2012) 124–134.

[41] W.J. van Ooij, D. Zhu, M. Stacy, A. Seth, T. Mugada, J. Gandhi, P. Puomi, Corrosion protection properties of organofunctional silanes - an overview, Tsinghua, Sci. Technol. 10 (2005) 639–664.

[42] S. Akbarzadeh, Y. Paint, M.-G. Olivier, A comparative study of different sol-gel coatings for sealing the plasma electrolytic oxidation (PEO) layer on AA2024 alloy, Electrochim. Acta 443 (2023) 141930.

[43] U. Tiringer, J.P.B. van Dam, S.T. Abrahami, H. Terryn, J. Kovač, I. Milošev, J.M. C. Mol, Scrutinizing the importance of surface chemistry versus surface roughness for aluminium / sol-gel film adhesion, Surf. Interf. 26 (2021) 101417.

[44] D. Wang, G.P. Bierwagen, Sol–gel coatings on metals for corrosion protection, Prog. Org. Coat. 64 (2009) 327–338.

[45] S. Akbarzadeh, L.B. Coelho, L. Dangreau, A. Lanzutti, L. Fedrizzi, M.G. Olivier, Self-healing plasma electrolytic oxidation (PEO) coating developed by an assembly of corrosion inhibitive layer and sol-gel sealing on AA2024, Corros. Sci. 222 (2023) 111424.

[46] L. Pezzato, M. Rigon, A. Martucci, K. Brunelli, M. Dabalà, Plasma electrolytic oxidation (PEO) as pre-treatment for sol-gel coating on aluminum and magnesium alloys, Surf. Coat. Technol. 366 (2019) 114–123.

[47] I. Milošev, B. Kapun, P. Rodič, J. Iskra, Hybrid sol–gel coating agents based on zirconium(IV) propoxide and epoxysilane, J. Sol-Gel Sci. Technol. 74 (2015) 447–459.

[48] L. Sopchenski, J. Robert, M. Touzin, A. Tricoteaux, M.G. Olivier, Improvement of wear and corrosion protection of PEO on AA2024 via sol-gel sealing, Surf. Coat. Technol. 417 (2021) 127195.

[49] H. Costenaro, A. Lanzutti, Y. Paint, L. Fedrizzi, M. Terada, H.G. de Melo, M. G. Olivier, Corrosion resistance of 2524 Al alloy anodized in tartaric-sulphuric acid at different voltages and protected with a TEOS-GPTMS hybrid sol-gel coating, Surf. Coat. Technol. 324 (2017) 438–450.

[50] S. Sharma, S. Sangal, K. Mondal, On the optical microscopic method for the determination of ball-on-flat surface linearly reciprocating sliding wear volume, Wear 300 (2013) 82–89.

[51] G. Yeshmanova, C. Blawert, M. Serdechnova, D.C.F. Wieland, M. Starykevich, E. Gazenbiller, D. Höche, D. Smagulov, M.L. Zheludkevich, Effect of electrolyte composition on the formation of PEO coatings on AA2024 aluminium alloy, Surf. Interf. 44 (2024) 103797.

[52] L. Moreno, M. Mohedano, R. Arrabal, E. Matykina, Development and screening of (ca-P-Si-F)-PEO coatings for biodegradability control of mg-Zn-ca alloys, J. Magnes. Alloy. 10 (2022) 2220–2237.

[53] A.C. Bouali, M. Serdechnova, K.A. Yasakau, A. Lutz, G. Wiese, H. Terryn, M.G. S. Ferreira, M.L. Zheludkevich, The role of cu-based intermetallic on the direct growth of a ZnAl LDH film on AA2024, J. Electrochem. Soc. 169 (2022) 081501.

[54] R.C. Zeng, L. Sun, Y.F. Zheng, H.Z. Cui, E.H. Han, Corrosion and characterisation of dual phase mg–Li–ca alloy in Hank's solution: the influence of microstructural features, Corros. Sci. 79 (2014) 69–82.

[55] M. Serdechnova, M. Mohedano, B. Kuznetsov, C.L. Mendis, M. Starykevich, S. Karpushenkov, J. Tedim, M.G..S. Ferreira, C. Blawert, M.L. Zheludkevich, PEO coatings with active protection based on in-situ formed LDH-Nanocontainers, J. Electrochem. Soc. 164 (2017) C36–C45.

[56] R.O. Hussein, X. Nie, D.O. Northwood, A. Yerokhin, A. Matthews, Spectroscopic study of electrolytic plasma and discharging behaviour during the plasma electrolytic oxidation (PEO) process, J. Phys. D. Appl. Phys. 43 (2010) 105203.

[57] R.H.U. Khan, A. Yerokhin, X. Li, H. Dong, A. Matthews, Surface characterisation of DC plasma electrolytic oxidation treated 6082 aluminium alloy: effect of current density and electrolyte concentration, Surf. Coat. Technol. 205 (2010) 1679–1688.

[58] W. Xue, Z. Deng, Y. Lai, R. Chen, Analysis of phase distribution for ceramic coatings formed by microarc oxidation on aluminum alloy, J. Am. Ceram. Soc. 81 (1998) 1365–1368.

[59] G. Lv, W. Gu, H. Chen, W. Feng, M.L. Khosa, L. Li, E. Niu, G. Zhang, S.Z. Yang, Characteristic of ceramic coatings on aluminum by plasma electrolytic oxidation in silicate and phosphate electrolyte, Appl. Surf. Sci. 253 (2006) 2947–2952.

[60] S. Sikdar, P.V. Menezes, R. Maccione, T. Jacob, P.L. Menezes, Plasma electrolytic oxidation (PEO) process—processing, Prop. Applic. Nanomater. 11 (2021) 1375.

[61] G. Lefèvre, M. Duc, P. Lepeut, R. Caplain, M. Fédoroff, Hydration of γ-alumina in water and its effects on surface reactivity, Langmuir 18 (2002) 7530–7537.

[62] M.J. Juan-Díaz, M. Martínez-Ibáñez, M. Hernández-Escolano, L. Cabedo, R. Izquierdo, J. Suay, M. Gurruchaga, I. Goñi, Study of the degradation of hybrid sol–gel coatings in aqueous medium, Prog. Org. Coat. 77 (2014) 1799–1806.

[63] J. Beardmore, X. Lopez, J.I. Mujika, C. Exley, What is the mechanism of formation of hydroxyaluminosilicates?, Sci. Rep. 2016 61. 6 (2016) 1–8.

[64] R. del Olmo, E. López, E. Matykina, U. Tiringer, J.M.C. Mol, M. Mohedano, R. Arrabal, Hybrid PEO/sol-gel coatings loaded with Ce for corrosion protection of AA2024-T3, Prog. Org. Coat. 182 (2023) 107667.

[65] C.L. Alexander, B. Tribollet, M.E. Orazem, Contribution of surface distributions to constant-phase-element (CPE) behavior: 1. Influence of roughness, Electrochim. Acta 173 (2015) 416–424.

[66] W. Liu, Y. Pu, H. Liao, Y. Lin, W. He, Corrosion and Wear behavior of PEO coatings on D16T aluminum alloy with different concentrations of graphene, Coatings 10 (2020) 249.

[67] M. Zhu, Y. Song, K. Dong, D. Shan, E.H. Han, Correlation between the transient variation in positive/negative pulse voltages and the growth of PEO coating on 7075 aluminum alloy, Electrochim. Acta 411 (2022) 140056.

[68] S. Amand, M. Musiani, M.E. Orazem, N. Pébère, B. Tribollet, V. Vivier, Constant-phase-element behavior caused by inhomogeneous water uptake in anti-corrosion coatings, Electrochim. Acta 87 (2013) 693–700.

[69] C. Liu, B. Qian, P. Hou, Z. Song, Stimulus responsive Zeolitic Imidazolate framework to achieve corrosion sensing and active protecting in polymeric coatings, ACS Appl. Mater. Interfaces 13 (2021) 4429–4441.

[70] R. Farrakhov, O. Melnichuk, E. Parfenov, V. Mukaeva, A. Raab, V. Sheremetyev, Y. Zhukova, S. Prokoshkin, Comparison of biocompatible coatings produced by plasma electrolytic oxidation on cp-Ti and Ti-Zr-Nb Superelastic alloy, Coatings 11 (2021) 401.

[71] S. Akbarzadeh, M. Ramezanzadeh, B. Ramezanzadeh, G. Bahlakeh, A green assisted route for the fabrication of a high-efficiency self-healing anti-corrosion coating through graphene oxide nanoplatform reduction by Tamarindus indiaca extract, J. Hazard. Mater. 390 (2020) 122147.

[72] B. Hirschorn, M.E. Orazem, B. Tribollet, V. Vivier, I. Frateur, M. Musiani, Determination of effective capacitance and film thickness from constant-phase-element parameters, Electrochim. Acta 55 (2010) 6218–6227.

[73] M. Javidi, H. Fadaee, Plasma electrolytic oxidation of 2024-T3 aluminum alloy and investigation on microstructure and wear behavior, Appl. Surf. Sci. 286 (2013) 212–219.

[74] Z. Rahmati, H. Jamshidi Aval, S. Nourouzi, R. Jamaati, An investigation on AA2024-15 wt%cu composite cladded on AA1050 with superb mechanical and tribological properties, CIRP J. Manuf. Sci. Technol. 39 (2022) 276–293.

[75] M.H. Staia, E.S. Puchi Cabrera, A. Iost, A. Zairi, S. Belayer, A. Van Gorp, Tribological response of AA 2024-T3 aluminium alloy coated with a DLC duplex coating, Tribol. Int. 85 (2015) 74–87.

[76] A.K. Mukhopadhyay, D. Chakraborty, M.V. Swain, Y.W. Mai, Scratch deformation behaviour of alumina under a sharp indenter, J. Eur. Ceram. Soc. 17 (1997) 91–100.